Bulletin of the Seismological Society of America, Vol. 107, No. 1, pp. 256–275, February 2017, doi: 10.1785/0120150301

Squeezing Kappa (κ) Out of the Transportable Array: A Strategy for Using Bandlimited Data in Regions of Sparse Seismicity

by Olga-Joan Ktenidou,* Walter J. Silva, Robert B. Darragh, Norman A. Abrahamson, and Tadahiro Kishida

Abstract The κ parameter (Anderson and Hough, 1984), and namely its site-specific component (κ_0), is important for predicting and simulating high-frequency ground motion. We develop a framework for estimating κ_0 and addressing uncertainties under the challenging conditions often imposed in practice: (1) low seismicity (limited, poor-quality, distant records); (2) limited-bandwidth data from the Transportable Array (TA; maximum usable frequency 16 Hz); and (3) low magnitudes (M_L 1.2–3.4) and large uncertainty in stress drop (corner frequency). We cannot resolve stress drop within the bandwidth, so we propose an approach that only requires upper and lower bounds on its regional values to estimate κ_0. To address uncertainties, we combine three measurement approaches (acceleration spectrum slope [AS]; displacement spectrum slope [DS]; and broadband spectral fit). We also examine the effect of crustal amplification, and find that neglecting it can affect κ_0 by up to 35%. DS estimates greatly exceed AS estimates. We propose a reason behind this bias, related to the residual effect of the corner frequency on κ_{AS} and κ_{DS}. For our region, we estimate a frequency-independent mean S-wave Q of 900 ± 300 at 9–16 Hz, and an ensemble mean κ_0 over all sites of 0.033 ± 0.014 s. This value is similar to the native κ_0 of the Next Generation Attenuation-West 2 ground-motion prediction equations, indicating that these do not need to be adjusted for κ_0 for use in southern Arizona. We find that stress-drop values in this region may be higher compared to estimates of previous studies, possibly due to trade-offs between stress drop and κ_0. For this dataset, the within-approach uncertainty is much larger than the between-approach uncertainty, and it cannot be reduced if the data quality is not improved. The challenges discussed here will be relevant in studies of κ for other regions with bandlimited data; for example, any region where data come primarily from the TA.

Introduction

Estimating ground motion at high frequencies is especially important for two classes of engineered structures: stiff structures with natural frequencies above 10 Hz, such as small concrete dams where the peak stresses may be controlled by high frequencies (Muto and Duron, 2015), and structures whose safety-related equipment is sensitive to ground shaking at frequencies above 20 Hz, such as nuclear power plants (PGE, 1988).

At high frequencies, the spectral amplitude of acceleration decays rapidly. Hanks (1982) first introduced f_{max} to model the frequency above which the spectrum decreases, whereas Anderson and Hough (1984) introduced the spectral decay factor (κ) to model the rate of the decrease. In its original definition, κ comprises site and path components. Anderson and Hough (1984) defined κ based on the observation that, above a given frequency, the amplitude of the Fourier acceleration spectrum (AS) decays linearly if plotted in linear–log space. κ for a given record at some epicentral distance R (termed κ_r) can be related to the slope (λ) of the spectrum (a) as $\kappa_r = -\lambda/\pi$, in which $\lambda = \Delta(\ln a)/\Delta f$. The same authors observed that measured κ_r values at a given station increase with distance. The zero-distance intercept of the κ trend with distance (denoted κ_0) is assumed to represent S-wave attenuation for vertical propagation through the geological structure beneath the station. The distance dependence reflects the incremental attenuation due to predominantly horizontal S-wave propagation through the crust from the source to the site. As a first approximation, the distance dependence is sometimes considered linear, so that

*Also at Helmholtz Centre Potsdam, GFZ German Research Centre for Geosciences, Helmholtzstrasse 6, 14467 Potsdam, Germany.

Table 1
Approaches Used for Estimating κ

Notation	Principle	Main References	Measurement/Computation	Frequency Range
κ_{AS}	High-frequency decay of the *S*-wave FAS for large magnitudes	Anderson and Hough (1984), Hough and Anderson (1988)	Direct measurement on the *S*-wave Fourier acceleration spectrum above f_c, where it is theoretically flat	Above f_c*
κ_{DS}	Low-frequency decay of the *S*-wave FAS for small magnitudes (strong trade-off with source)	Biasi and Smith (2001)	Direct measurement on low-frequency part of the Fourier displacement spectrum (below f_c), where it is theoretically flat	Below f_c
κ_{BB}	Inversion of the entire frequency band of the spectrum	Anderson and Humphrey (1991), Humphrey and Anderson (1992), Electric Power Research Institute (EPRI) (1993), Schneider *et al.* (1993), Silva *et al.* (1997), Edwards *et al.* (2011)	Broadband inversion of the entire spectrum for source, path, and site terms (usually for moment, f_c, and κ_0)	Entire band

FAS, Fourier amplitude spectra; AS, acceleration spectrum; DS, displacement spectrum; BB, broadband.
*f_c, source corner frequency.

κ_r can be written as $\kappa_r = \kappa_0 + mR_e$. A discussion on distance dependence, which can vary greatly from the linear assumption, can be found in Ktenidou *et al.* (2014).

Though the physics are still not completely understood, in current applications, κ_0 is primarily assumed to describe site attenuation due to local geological conditions a few hundreds of meters to a few kilometers beneath the site under study (Anderson and Hough, 1984; Campbell, 2009). It is used as a site parameter for describing high-frequency motion in various applications, including the simulation of ground motion and the creation and adjustment of ground-motion prediction equations (GMPEs) from one region to another (Biro and Renault, 2012). In the latter context, κ_0 (as opposed to V_S) can be the dominant factor in characterizing the response of rock sites (Laurendeau *et al.*, 2013), particularly in regions of low seismicity and stable continental regions.

Recently, existing approaches for estimating κ_0 from seismic records were grouped into a taxonomy (Ktenidou *et al.*, 2014). κ_0 values derived using different methods may or may not be consistent, and this uncertainty may have significant effects on the estimated high-frequency ground motion. The existing approaches have been categorized based on the frequency range over which κ is measured (Table 1). There are bandlimited approaches, in which κ is estimated from the slope of the AS above the source corner frequency (denoted AS), or from the slope of the displacement spectrum below the corner frequency. There are also broadband approaches, where the full frequency range of the Fourier amplitude spectra (FAS) is fit to an omega-square spectrum (e.g., Boore, 1983) both above and below the corner frequency (denoted BB). In the BB method, the source, site, and path parameters in the omega-square spectrum are estimated by regression on the log FAS. Past studies have shown that κ_0 estimates have very large uncertainty; they can vary significantly across studies and methods as well as within a given study or method (Ktenidou *et al.*, 2014).

An estimate of κ_0 and its uncertainty may be particularly important for low-seismicity regions, where GMPEs are often developed by adjusting GMPEs from active regions (host regions) for the known differences in the V_{S30} and κ_0 values between the host region and the target region (e.g., Campbell, 2003, 2004). The usual practice is to infer the target κ_0 value from existing empirical κ_0–V_{S30} correlations. However, the uncertainty is large, owing to the scatter in existing correlations (e.g., Van Houtte *et al.*, 2011). Scatter may be due to differences in regions, frequency band, or approach (Ktenidou *et al.*, 2014). Also, the typically assumed continuous decrease of κ_0 at very high V_S values may be erroneous, leading to underestimation of κ_0 and overestimating of the adjusted high-frequency ground motion (Ktenidou *et al.*, 2015). The preferred approach is to estimate values of site-specific κ_0 based on recordings in the site region. In practice and particularly for low-activity regions, it can be very difficult to achieve an accurate site-specific κ_0 estimate due to several reasons: scarcity of close-in recordings, low signal-to-noise ratio (SNR) at greater distances or lower magnitudes, larger uncertainties in magnitude and location estimation, and the larger uncertainty in the source corner frequency for smaller earthquakes.

Although κ_0 can be important in characterizing high-frequency ground motion, few studies have attempted to estimate it in such low-seismicity regions using region-specific recordings. This study was motivated by the need for site characterization in southern Arizona that arose within the Southwestern United States Ground Motion Characterization Project (SWUS GMC), which developed ground-motion models for application to nuclear power plants in Arizona and California. Several limitations make this study challenging: (1) as in most low-seismicity areas in the United States, data in southern Arizona come primarily from the recently deployed Transportable Array (TA), which has band limitations, namely a highest usable frequency (HUF) of 16 Hz. (2) Southern Arizona (Fig. 1a) is a region of low seismicity, and the available seismic records are few and recorded over a large range of distances (10–300 km); uncertainty in magnitude and location may be larger than usual. These factors increase the correlations between the site and path

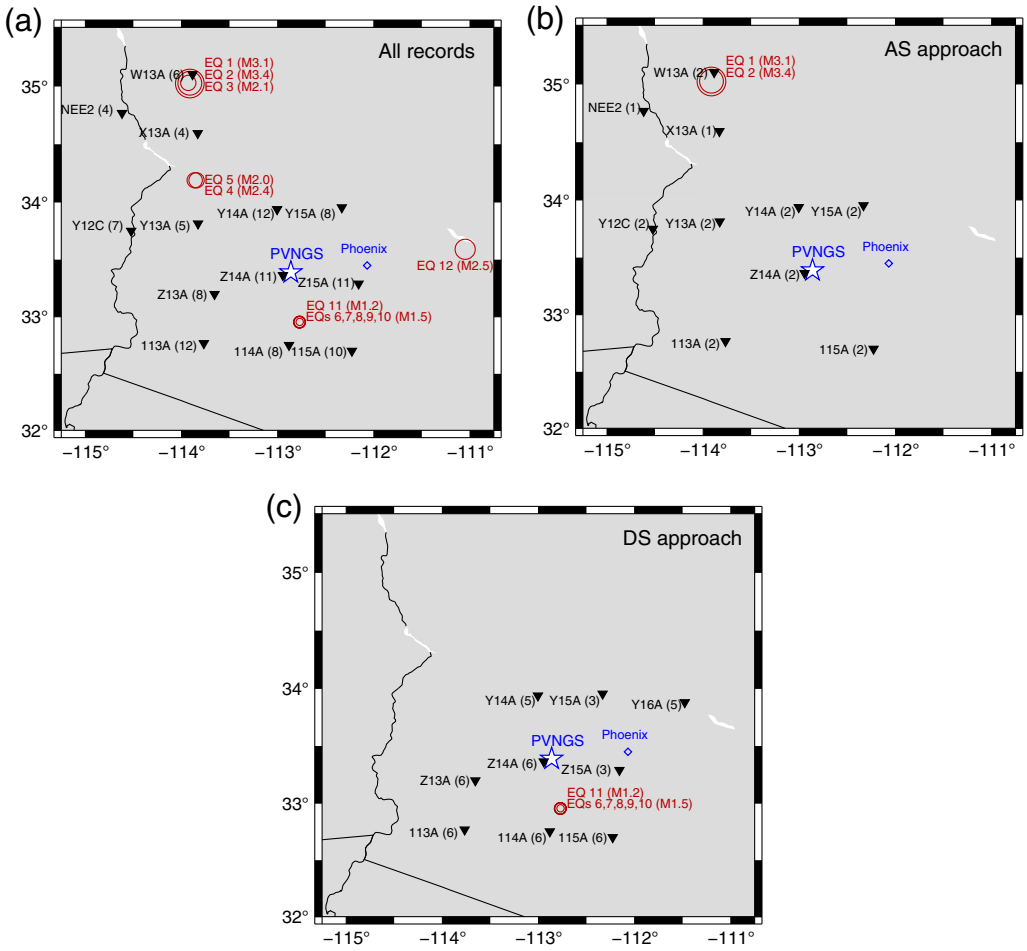

Figure 1. (a) Earthquake epicenter locations (circles) and station locations (triangles), with number of records per station in parenthesis. Location of site under study (Palo Verde Nuclear Generating Station [PVNGS]) is also shown. (b) The events analyzed with the acceleration spectrum (AS) approach and the stations that recorded them. (c) Same as (b), for the displacement spectrum (DS) approach. The color version of this figure is available only in the electronic edition.

components of attenuation. (3) The magnitudes of the events (**M** 1.2–3.4) are smaller than optimal for the classical κ_{AS} estimation approach, and higher than optimal for the displacement spectrum (DS) approach. (4) The range of available stress drop estimates from previous studies for the region under study is very wide (1–50 bar), which leads to large uncertainty as to the range of source corner frequencies. The data provide little bandwidth at high frequencies to resolve and decouple source, path, and site effects, and ultimately constrain κ_0. (5) Within the available bandwidth (<16 Hz), there may be site resonance patterns coming from shallow soil layers, which may interfere with the measurement of κ. These cannot be avoided by choosing a higher frequency range. We address these limitations by combining three measurement approaches (AS, DS, and BB) to estimate an upper and lower value of κ_0 for the region, together with estimates of regional attenuation (Q) and the stress parameter.

Many previous research-driven studies worked with rich datasets and helped understand various aspects of κ_0 (e.g., Van Houtte *et al.*, 2011, 2014; Kilb *et al.*, 2012). This study focuses on the problem of estimating region-specific κ_0 values in low-seismicity regions often faced in practice and suggests a way to combine and expand existing approaches to capture the mean and scatter of κ_0 using local and regional data rather than global correlations of κ_0 with V_{S30}. To our knowledge, this is also the first study to compute κ_0 from TA data. Considering that for many regions in the central and eastern United States (CEUS), the TA is the primary source of data, the methodology proposed here should be relevant to κ_0 estimation for other regions of CEUS.

Study Region and Ground-Motion Data

Our study region is southern Arizona. As for many less-active regions in the United States, all the available data useful for κ estimation come from stations in the TA deployment (USArray). There are 14 stations used in this study, and these are listed in Table 2, along with their V_{S30} values. The V_S estimation from the site characterization (including spectral analysis of surface waves measurements) is described in detail in Kishida *et al.* (2014). Figure 1a shows the station locations (dark triangles) and epicenters of the events

Table 2
List of Stations

Station Name	V_{S30} (m/s)	Number of Events Recorded	Event Magnitude Range	Record Distance Range (km)	Number of Events Used for κ_{AS}	Number of Events Used for κ_{DS}
113A	1237	12	1.5–3.4	96–250	2	6
114A	398	8	1.2–2.4	28–183	-	6
115A	460	10	1.2–3.4	59–301	2	6
NEE2	401	4	2.0–3.4	69–96	1	-
W13A	660*	6	2.0–3.4	9–101	2	-
X13A	425*	4	2.0–3.1	45–49	1	-
Y12C	660*	7	2.1–3.4	152–152	2	-
Y13A	560	5	2.0–3.4	42–135	2	-
Y14A	520	12	1.5–3.4	82–147	2	5
Y15A	566	8	1.5–3.4	119–189	2	3
Y16A	1028	5	1.5–1.5	158–159	-	5
Z13A	689	8	1.5–2.4	88–111	-	6
Z14A	524	11	1.2–3.4	50–206	2	6
Z15A	407	11	1.5–3.1	69–251	-	3

*V_{S30} assigned by proxy.

Table 3
List of Earthquakes

Code	EQID	Origin Time (yyyy/mm/dd hh:mm)	Magnitude*	Latitude (°)	Longitude (°)	Depth (km)
EQ1	1267	2008/01/05 23:45	M_L 3.10	35.0230	−113.9140	1.00
EQ2	1268	2008/01/17 22:00	M_L 3.40	35.0200	−113.9140	1.00
EQ3	1269	2008/01/20 17:28	M_L 2.10	35.0260	−113.9290	1.00
EQ4	1270	2008/07/24 14:05	M_L 2.40	34.1880	−113.8440	6.00
EQ5	1271	2008/08/03 09:53	M_L 2.00	34.1880	−113.8620	7.00
EQ6	1272	2008/11/29 01:48	M_L 1.50	32.9520	−112.7740	13.00
EQ7	1273	2008/11/29 07:10	M_L 1.50	32.9530	−112.7740	13.00
EQ8	1274	2008/11/29 07:11	M_L 1.50	32.9550	−112.7720	13.00
EQ9	1275	2008/11/29 07:22	M_L 1.50	32.9550	−112.7710	13.00
EQ10	1276	2008/11/29 16:21	M_L 1.50	32.9540	−112.7700	13.00
EQ11	1277	2008/11/29 16:22	M_L 1.20	32.9550	−112.7700	13.00
EQ12	1278	2012/02/03 02:42	M_D 2.50	33.5905	−111.0490	13.87

*M_L is local and M_D is duration magnitude.

(circles), along with the site of interest (Palo Verde Nuclear Generating Station [PVNGS]). There are 12 earthquakes located in Arizona recorded at distances less than 300 km (Table 3). Magnitudes range from M_L 1.2 to 3.4. All magnitudes are local (events 1–11 from 2008) except for the most recent event (event 12 from 2012), for which we have duration magnitude; the magnitudes are assumed to be equivalent to M_w at $\mathbf{M} < 3.5$. Magnitude estimates are from J. Young (Arizona Geological Survey Earthquake Information Center, personal comm., 2013). We do not have information on location errors, but this absence is part of the problem we are addressing in this study. The recordings were visually evaluated for record quality and noise, leaving 80 three-component recordings after rejecting 37 recordings. Figure 2a shows the magnitude–distance distribution of the records.

The data processing took into account the band limitation. All TA stations used in this study are BB velocity sensors with a sampling rate of 40 Hz, and so the Nyquist frequency for all records is 20 Hz. The anti-alias filter applied near 80% of the Nyquist further reduces the HUF to 16 Hz. The response of the sensor is flat between 0.01 and 16 Hz. The velocity time series were corrected by multiplying the count with the gain values without applying any instrument correction within this frequency band. Next, the standard Pacific Earthquake Engineering Research Center (PEER) algorithm for baseline correction was applied (Chiou *et al.*, 2008; Ancheta *et al.*, 2013), and the data processing followed the PEER procedure described in Ancheta *et al.* (2013). At frequencies below 0.5 Hz, microseism noise is dominant in most recordings. A five-pole acausal high-pass filter was applied; the filter corner frequency was selected based on noise level, and for most components was near 0.5 Hz. No additional low-pass filter was applied, due to the anti-alias filter at 16 Hz. The integration of filtered velocity time series into acceleration was performed in the frequency domain. *S*-arrival times were selected by inspection of acceleration and displacement time histories of all three components. For the *S*-wave window duration, a standard value was

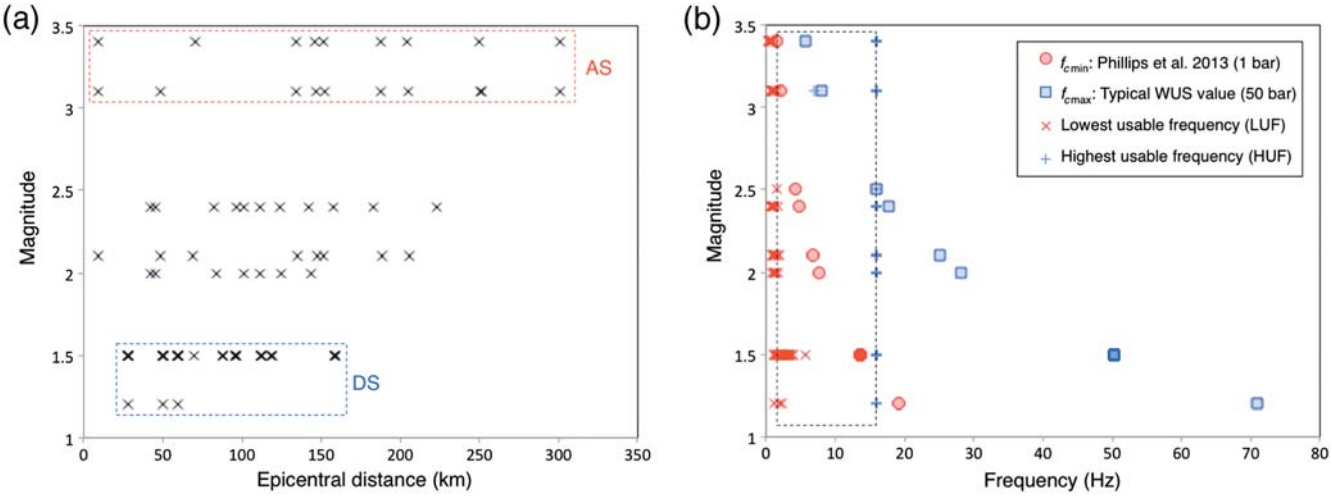

Figure 2. (a) Magnitude versus distance distribution of the dataset. The top box indicates the records used for the AS approach, and the bottom box those used for the DS approach. All records were used for the broadband (BB) approach. (b) The range of possible source corner frequencies assuming stress drops of 1 and 50 bars (circles), and the highest and lowest usable frequencies of each record (crosses). The dashed box indicates the typical usable frequency range of the records, based on noise level, sampling rate, and filtering. The color version of this figure is available only in the electronic edition.

first attributed automatically as a function of hypocentral distance and magnitude, and then visually checked so that the *S*-wave time window contained the strongest part of the motion in each record. Where possible, pre-event noise windows were selected; if unavailable, noise windows were taken from the end of the record, as late as possible in the coda portion of the waveform. The *S*-wave and noise windows were then tapered, zero-padded to ensure a constant record length, and Fourier-transformed to produce FAS. The FAS have a common frequency step to facilitate the computation of the SNR. Acceleration and displacement seismograms are also calculated by multiplying and dividing the velocity FAS by ω^2, in which ω is the angular frequency ($2\pi f$).

Available Approaches

We briefly describe some of the main approaches available, namely the bandlimited AS and DS approaches and the BB fit approach, before suggesting a strategy for combining them in our case study.

AS Approach

This approach follows from the original definition of κ. $\kappa_{r_{AS}}$ is measured as the slope of the high-frequency part of the *S*-wave acceleration FAS when it is plotted in log–linear space. The high-frequency decay of the FAS is fitted with a straight line with least-squares linear regression between frequencies f_1 and f_2. To avoid trade-off between site and source effects, the frequency range chosen ($Df = f_2 - f_1$) must lie above the source f_c, which can be taken as

$$f_c = 4.9 \times 10^6 \beta \left(\frac{\Delta\sigma}{M_0}\right)^{\frac{1}{3}} \quad (1)$$

(e.g., Aki, 1967; Brune, 1970, 1971; Boore 1983), in which β is the crustal shear-wave velocity at the source, $\Delta\sigma$ is the stress drop, and M_0 is the seismic moment computed after Hanks and Kanamori (1979) as

$$M_0 = 10^{1.5\mathbf{M}+16.05}, \quad (2)$$

in which **M** is the moment magnitude (we use the local and distance magnitudes of Table 3 as **M** here).

The AS approach is typically used for relatively large magnitudes, where bandwidth is normally available above f_c, even with large uncertainty in the $\Delta\sigma$. For instance, assuming a typical value of $\beta = 3.5$ km/s, a typical estimate of f_c could range from 0.25 to 1.1 Hz for **M** 5.0 and from 0.8 to 3.6 Hz for **M** 4.0, if $\Delta\sigma$ varies from 1 to 100 bars. So one can easily use **M** 5.0 records above 2 Hz and **M** 4.0 records above 4 Hz, avoid the f_c in computing $\kappa_{r_{AS}}$, and still maintain enough bandwidth between f_c and the HUF of the data. However, if one needs to use lower magnitudes, the uncertainty in stress drop has a stronger effect on the choice of frequency; for example, for **M** 3.0, f_c it could range from 2.4 to 11 Hz for 1–100 bars, for **M** 2.0 from 8 to 35 Hz, and for **M** 1.0 from 24–112 Hz. So above **M** 2.0, and depending on the HUF, the AS approach could only be used for very low values of $\Delta\sigma$; and one problem is that actually the estimation of such small $\Delta\sigma$ values may in turn be contaminated by the κ effect. For magnitudes below **M** 2.0, the AS approach is generally not used.

The $\kappa_{r_{AS}}$ values include the effect of damping along the path (Q), and so we need to extrapolate to zero epicentral distance to obtain the site-specific $\kappa_{0_{AS}}$. In doing so, we generally assume Q is frequency independent and constant with depth. Based on the data at hand in any given study, the

simplification of linear dependence with distance may or may not be appropriate in performing this extrapolation.

Some steps for applying the AS approach were outlined in Ktenidou *et al.* (2013, 2016). The main considerations for the chosen frequency range (f_1 to f_2) are: (1) the FAS should be corrected for crustal amplification, unless it is flat within the range; (2) within this range, κ should not be strongly biased by site-specific shallow resonances (Parolai and Bindi, 2004); (3) the instrument response can be considered flat within the range, and the latter should be unaffected by the anti-alias; (4) the range has an acceptable SNR (e.g., 3 or greater); (5) the range is of adequate width (in this severely bandlimited case, as a compromise, we set the minimum to 7 Hz). The two horizontal components can be combined into the geometric mean or used separately.

DS Approach

Biasi and Smith (2001) introduced the DS approach to allow the use of small events, which cannot generally be used in the AS approach, as explained above. For instance, for events of **M** 0, assuming self-similarity, the f_c can range from 75 to 355 Hz for $\Delta\sigma$ varying from 1 to 100 bar. In such cases, it is generally impossible to measure $\kappa_{r_{\mathrm{AS}}}$ on the acceleration FAS above f_c. Instead, $\kappa_{r_{\mathrm{DS}}}$ can be measured on the displacement FAS below the f_c and represent the departure of the displacement FAS from the horizontal over the chosen range of frequencies (in this case, f_1 to f_2 lie below the source f_c and are chosen with similar criteria as in the AS method—see e.g., Ktenidou *et al.*, 2016). For very small events, for example **M** 0, one can easily be sure of working below f_c regardless of $\Delta\sigma$. One of the advantages of this approach is that we are more confident of the assumption underlying the DS approach (i.e., that the displacement FAS for the source is flat in a measurement window somewhere below f_c) than in the assumption underlying the AS approach (i.e., that the acceleration FAS is flat in a measurement window somewhere above f_c), because the latter requires the ω^{-2} assumption to hold true. Similar to the AS approach, in the DS approach we must extrapolate measured $\kappa_{r_{\mathrm{DS}}}$ values to zero distance to estimate the site-specific $\kappa_{0_{\mathrm{DS}}}$, and similar considerations apply for the chosen frequency band.

Broadband Approach

Several BB approaches exist such as Anderson and Humphrey (1991), Humphrey and Anderson (1992), Silva *et al.* (1997), and others, where data are inverted for seismological parameters using different numerical schemes such as grid searches and nonlinear regressions. Here we use the inversion method of Schneider *et al.* (1993) and Silva *et al.* (1997) as described below.

In the BB method, a parametric form of the FAS is fit to the observed FAS over the full frequency range. In this approach, κ_0 is one of the parameters estimated by regression. Kishida *et al.* (2014) fit the FAS to the following form:

$$\begin{aligned}\ln(\mathrm{FAS}_{ij}(f)) = {} & \mathrm{Const} + \ln(M_{0_i}) - \ln(R1_{ij}) \\ & + \ln\left(\frac{4\pi^2 f^2}{(1+(\frac{f}{f_{ci}})^2)}\right) - \frac{R_{ij}\pi f}{\beta Q_0 f^{\eta}} \\ & + \ln(\mathrm{Amp}_j(f)) - \pi\kappa_{0j} f, \end{aligned} \tag{3}$$

in which i is the earthquake index, j is the recording index, $\mathrm{FAS}_{ij}(f)$ is the vector sum of the FAS for the two horizontal components, M_0 is the seismic moment of the ith earthquake, f_{ci} is the corner frequency of the ith earthquake, R_{ij} is the rupture distance from earthquake i to station j, and β is the shear-wave velocity at the source depth, and

$$\mathrm{Const} = \ln\left(\frac{0.778\times 10^{-20}}{4\pi\beta^3\rho}\right), \tag{4}$$

$$\ln(\mathrm{Amp}_j(f)) = a_j f^3 + b_j f^2 + c_j f + d_j, \tag{5}$$

$$R1_{ij} = \begin{cases} R_{ij} & \text{if } R_{ij} < R_C \\ R_C\sqrt{\frac{R_{ij}}{R_C}} & \text{if } R_{ij} \geq R_C \end{cases}, \tag{6}$$

$$Q(f) = Q_0 \times f^n. \tag{7}$$

The model shown in equation (3) corresponds to an omega-square spectrum with the geometrical spreading set at -1 for distances less than R_C and at -0.5 for distances greater than R_C.

The free parameters in the model are the corner frequencies for each earthquake (f_{ci}), the Q terms for the region (Q_0 and η, equation 7), the site amplification terms (a_j, b_j, c_j, d_j), and the site κ_0 (κ_{0j}) for each site or site class. Given sufficient data, these parameters can be estimated by ordinary least-squares regression or they can be constrained based on other studies. As there can be strong correlations between the estimated parameter values, it is important that any constraints on the parameters be based on consistent parameters sets. For example, if the Q is constrained from other studies, then it needs to be from a study that used geometrical spreading coefficients that are consistent with the -1 and -0.5 assumed here.

Linear-Elastic Crustal Amplification

In all three approaches, the FAS are first corrected for crustal amplification through division of the FAS of the recorded ground motion by the site-specific transfer functions. The transfer functions represent linear-elastic (zero damping) amplification from the source depth to the ground surface at the site. The V_S profiles of the upper layers for each site are given by Kishida *et al.* (2014) and shown in Figure 3a. These individual profiles were grouped into two classes, one stiff soil ($V_{S30} \leq 670$ m/s, with site Z14A chosen as representative)

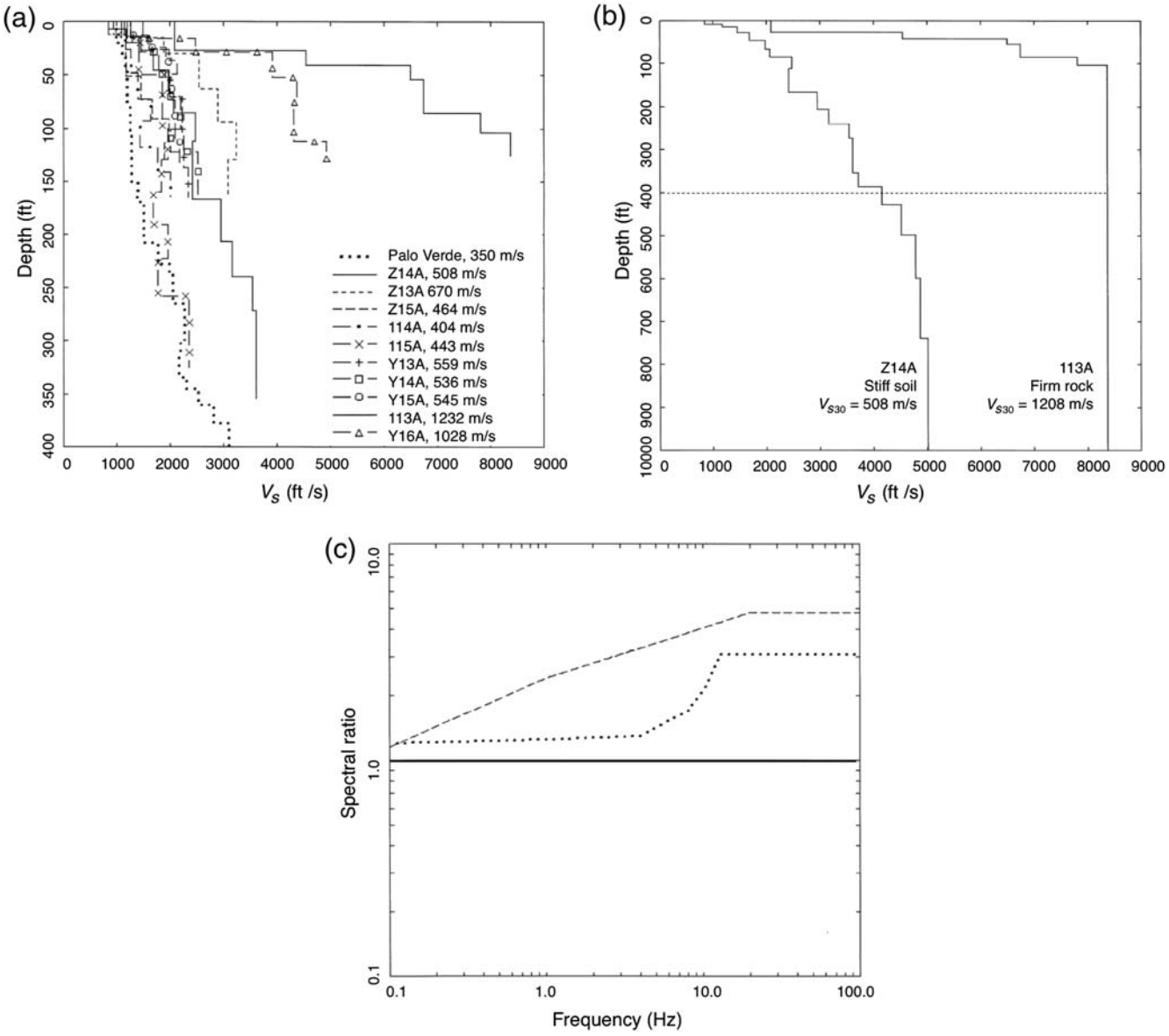

Figure 3. (a) The measured V_S profiles per station down to 130 m. (b) The chosen regional profiles for stiff soil and firm rock, down to 330 m. (c) Linear-elastic amplification for stiff soil (dashed line) and firm rock (dotted line) with respect to unity (solid line). Measuring κ_r below 10 Hz is affected by the slope in the amplification function, leading to underestimation, especially between 4 and 10 Hz for rock sites.

and one firm rock ($V_{S30} > 670$ m/s, with site 113A chosen as representative). These two near-surface profiles were appended onto a generic profile appropriate for the western United States (WUS; Kamai *et al.*, 2013) and extrapolated to 10 km depth (where the source region is assumed) with $\beta = 3.5$ km/s (Fig. 3b). For each class, a class-specific amplification factor was computed (Fig. 3c), with which all FAS recorded on that class of site were then corrected.

A New Strategy

We devise a strategy to use the AS and DS approaches without resolving the f_c uniquely from the data, but instead using upper and lower limits on the stress drop ($\Delta\sigma$). We demonstrate this in Figure 2b. From the scarce literature on stress drop in this region, we choose $\Delta\sigma_{\max} = 50$ bars as the upper bound value; this is a typical value for large events (**M** 7.5) in western North America according to Atkinson and Silva (1997). We choose as lower bound value $\Delta\sigma_{\min} = 1$ bar, which is the mean computed by Phillips *et al.* (2013) for smaller earthquakes (**M** 2.1–5.9) recorded by the TA for the WUS. Figure 2b shows the f_c values for these limit $\Delta\sigma$ values, which we call $f_{c\,\max}$ and $f_{c\,\min}$, respectively, and the usable bandwidth of the data, between the lowest useable frequency (LUF) and HUF (dashed box).

To use the AS method, we need enough of a frequency band above f_c for a stable estimate of the slope of the FAS. The most conservative estimate of the available bandwidth

for AS is between $f_{c\,\max}$ and HUF, and this exists only for the largest events (**M** 3.1 and 3.4). For these magnitudes, from equations (1) and (2), f_c equals 8 and 6 Hz, respectively. Allowing some bandwidth above $f_{c\,\max}$, we select the band from 9 to 16 Hz to estimate κ_{AS}.

Conversely, to use the DS method, f_c must be high enough to not interfere with the slope of the displacement FAS. The most conservative estimate of the available bandwidth for DS is between LUF and $f_{c\,\min}$. From Figure 2b, we see that there is only available bandwidth below $f_{c\,\min}$ for the smallest events (**M** 1.2 and 1.5), for which equations (1) and (2) give f_c of 20 and 14 Hz, respectively. We select the band from 4 to 16 Hz to estimate κ_{DS}.

For earthquakes between **M** 1.5 and 3.1, we cannot be sure that slope inflection caused by f_c would not affect κ_{AS} and κ_{DS}, and so for them we can only fit the full spectral shape (BB approach), and we use the imported stress-drop bounds to bound results of the inversion. In the end, the AS and DS approaches can be combined in a conservative way for the smallest and largest events, without a need to compute $\Delta\sigma$, whereas the BB approach can be applied to the entire dataset.

We make a clear distinction between the estimation of κ_r and κ_0 using the different methods. The goal is to estimate κ_0, the zero-distance, high-frequency decay factor. The AS and DS methods make individual estimates of κ_r by fitting individual FAS recorded at epicentral distance R_e. These κ_r estimates must then be interpreted to derive a model for the distance dependence of κ_r and estimate κ_0 at $R_e = 0$. The BB approach, on the other hand, corrects for attenuation along the path and yields κ_0.

Analysis and Results

Combining the AS and DS Approach

The stations and events used in the AS approach are shown in Table 2 and Figure 1b. Epicentral distances for these records span the range from 5 to 300 km. Assuming $\Delta\sigma_{\max}$, $\kappa_{r_{\mathrm{AS}}}$ is measured above $f_{c\,\max}$ in the 9–16 Hz on each acceleration FAS individually, for a total of one or two events per station, and for two horizontal components (two or four FAS per station). Figure 4a and 4c are examples of acceleration FAS for the same event recorded at different sites. The assumed $\Delta\sigma_{\max}$ gives $f_{c\,\max} = 6$ Hz, which may be related to the break in the FAS present in both sites (black solid line). Figure 4b shows the $\kappa_{r_{\mathrm{AS}}}$ results with distance computed in the 9–16 Hz range (above $f_{c\,\max}$) for each individual FAS (small crosses). The station name and V_{S30} value are included in the figure in parenthesis; an asterisk indicates V_{S30} values assigned by proxy. Station Z14A is underlined because it is the closest one to the PVNGS site. Because there are very few events per site, we also apply another approach: we measure $\kappa_{r_{\mathrm{AS}}}$ on a single FAS per station, which is calculated by logarithmically stacking all individual FAS per station. The stacking is used to improve the SNR and smooth over individual FAS differences, capturing the general trend of the decay in a more robust way. Normally, it is not acceptable to stack FAS with different f_c. We do it here because we are focusing on a segment of the FAS (9–16 Hz) that we have shown to be above the f_c for all FAS concerned. By adding the FAS logarithmically for those segments, we derive a slope that is the mean of the segment slopes regardless of their different amplitudes. In Figure 4b and 4d, the large bold crosses indicate the $\kappa_{r_{\mathrm{AS}}}$ results for the stacked FAS per station. The κ_r estimates derived from stacked FAS appear more robust than individual FAS measurements. Finally, note the break in the FAS observed around 2.5 Hz for site 113A. This is not visible for site W13A, and so it is likely not related to the source. If one were to assume a lower stress drop according to which the 2.5 Hz break was the source f_c, then $\kappa_{r_{\mathrm{AS}}}$ could be measured, for example, in the 5–16 Hz range. In that case, $\kappa_{r_{\mathrm{AS}}}$ would be biased low, including a negative value at close distance (gray circles in Fig. 4d). This is an example of the effect of measuring $\kappa_{r_{\mathrm{AS}}}$ too close to the f_c. Based on these observations, we believe that although we cannot resolve $\Delta\sigma$, it is likely much higher than $\Delta\sigma_{\min}$ and closer to $\Delta\sigma_{\max}$ (close to 50 bar).

In Figure 4a, let us focus on the scatter of $\kappa_{r_{\mathrm{AS}}}$ values with epicentral distance under the $f_{c\,\max}$ assumption. Though the stacking gives a more robust value of $\kappa_{r_{\mathrm{AS}}}$ per station, the scatter in the κ_r estimates versus distance remains large. Numerous reasons may lie behind this scatter: (1) the severe limitation in the HUF (16 Hz) and the small overall bandwidth ($Df > 7$ Hz); (2) the different site conditions, all sites except 113A (rock) have V_{S30} values around 500 ± 50 m/s, so it is reasonable that values for 113A are lower; (3) at some sites, there may be some distortion in the FAS due to high-frequency (shallow layer) resonances, which may bias the measurement of κ (Parolai and Bindi, 2004). This is likely the case for Y15A in Figure 4b. To confirm, we computed empirical horizontal-to-vertical spectral ratios (HVSRs) after Lermo and Chávez-García (1993) for coda as well as *S*-wave windows to check for site resonances at all sites. The high $\kappa_{r_{\mathrm{AS}}}$ measured for Y15A in the 9–16 Hz range may be due to the strong downgoing trend in the shape of the HVSR in that frequency range (dashed box in Fig. 5), which most likely biases κ high. On the contrary, for site 113A, there are no peaks in the frequency range of interest and the transfer function is practically flat. Hence, we infer that this low $\kappa_{r_{\mathrm{AS}}}$ for 113A is probably not biased by a site resonance. It is important to stress here that in this method it is not the level of amplification but the shape of the amplification function (peak succession) that can distort the FAS shape and cause bias to κ estimation. A flat transfer function between f_1 and f_2 would not affect κ no matter what the amplification level. The importance of amplification and its effect on the measurement of attenuation is also stressed by Ktenidou *et al.* (2016) and Ktenidou and Abrahamson (2016), using examples from the Next Generation Attenuation-East (NGA-East) project. Those authors suggest that $\kappa_{0_{\mathrm{AS}}}$ is likely the net effect of site attenuation and site amplification.

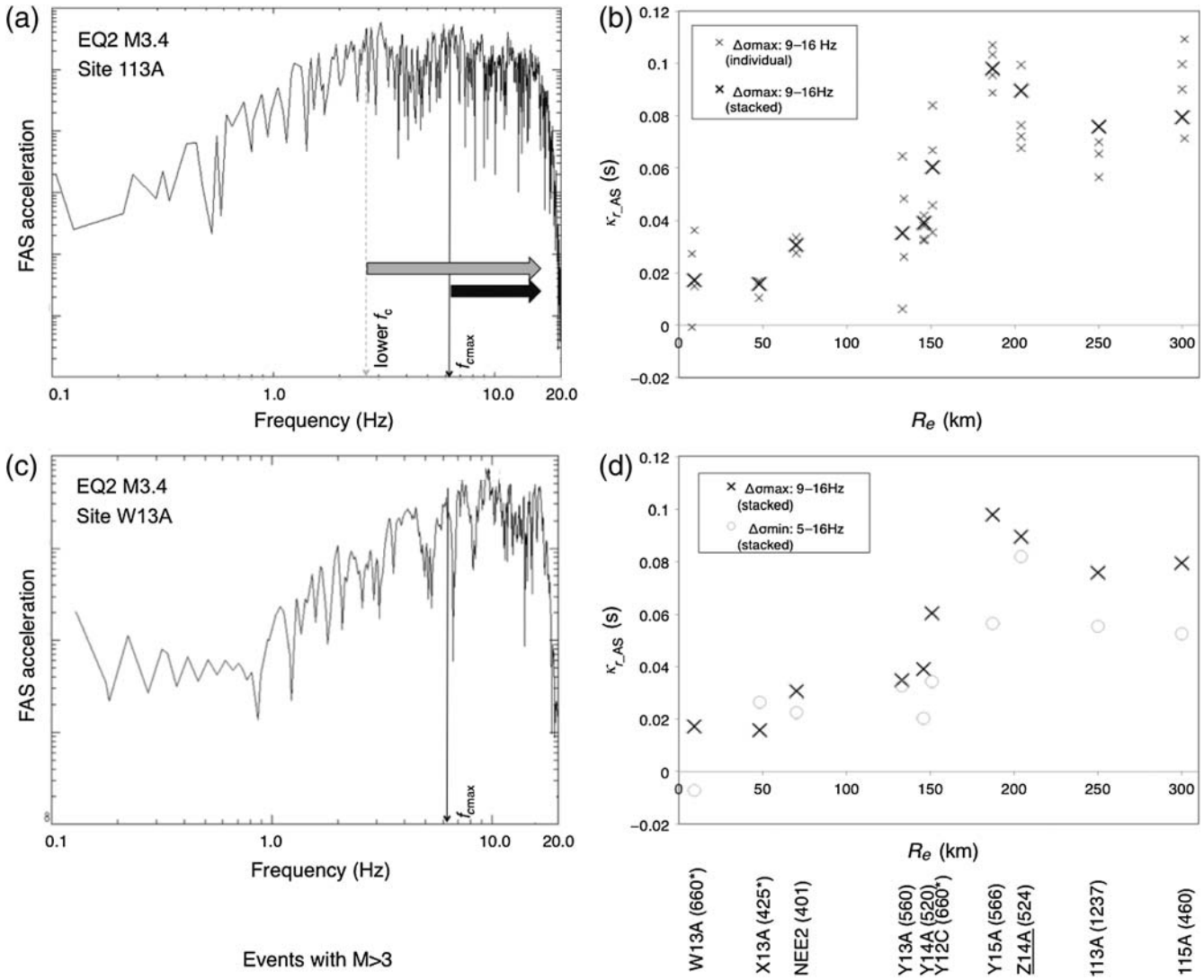

Figure 4. (a) An example of the acceleration Fourier amplitude spectra (FAS) at site 113A for an **M** 3.4 event. $f_{c\,\max}$ (black solid line) and a lower f_c (gray dashed line) that may interpret the break in the FAS is also shown. (b) $\kappa_{r_{AS}}$ results versus distance for individual-record FAS (large crosses) and stacked FAS (small crosses) computed assuming $f_{c\,\max}$. (c) Acceleration FAS for the same **M** 3.4 event at site W13A. Because the 2.5 Hz break is not present here, it cannot be source related, and the 6 Hz break at $f_{c\,\max}$ is likely nearer to the source f_c. (d) Comparison of $\kappa_{r_{AS}}$ results for stacked FAS assuming $f_{c\,\max}$ (crosses) and the lower f_c (circles); assuming the lower f_c biases results downward. Names and V_{S30} values of stations are also shown.

For the DS approach, the stations and events used are listed in Table 2 and Figure 1c. Most recording stations lie within 120-km epicentral distance from the source. Figure 6a is an example of acceleration FAS at hard site 113A, and Figure 6c shows the displacement FAS. The assumed $\Delta\sigma_{\min}$ gives $f_{c\,\min} = 16$ Hz (black solid line), which coincides with the HUF, and $\kappa_{r_{DS}}$ is measured below that from 4 to 16 Hz. Based on the location information available and for the purpose of this study, we consider the hypocenters for all six events to be collocated within their uncertainty. Because these events also have very similar and small magnitudes, we stack all FAS per station (i.e., the FAS segments below $f_{c\,\min}$), combining events and components. This will improve the SNR for these very small events and smooth over differences in individual FAS to obtain a more robust estimate of the overall attenuation. We logarithmically stack the displacement FAS for all earthquakes and for both horizontal components at each site (i.e., a total of 12 FAS for a site, which recorded all six earthquakes) and measure $\kappa_{r_{DS}}$ per station (small crosses in Fig. 6b). The scatter with distance is large above 70 km, so in an effort to smooth $\kappa_{r_{DS}}$ further, we take the stacking further and combine nearby sites according to epicentral distance (we choose bins of 0–40 km, 40–80 km, 80–120 km, and 120–160 km to group sites). All FAS are stacked for each distance bin, and then $\kappa_{r_{DS}}$ is estimated for each group of sites, that is, distance bin (large bold crosses in Fig. 7c,d). The stacking achieved more robust results at longer distances. Finally, we consider other possible interpretations of $\Delta\sigma$. One could interpret the break in the FAS in Figure 6a (gray dashed line) as a possible

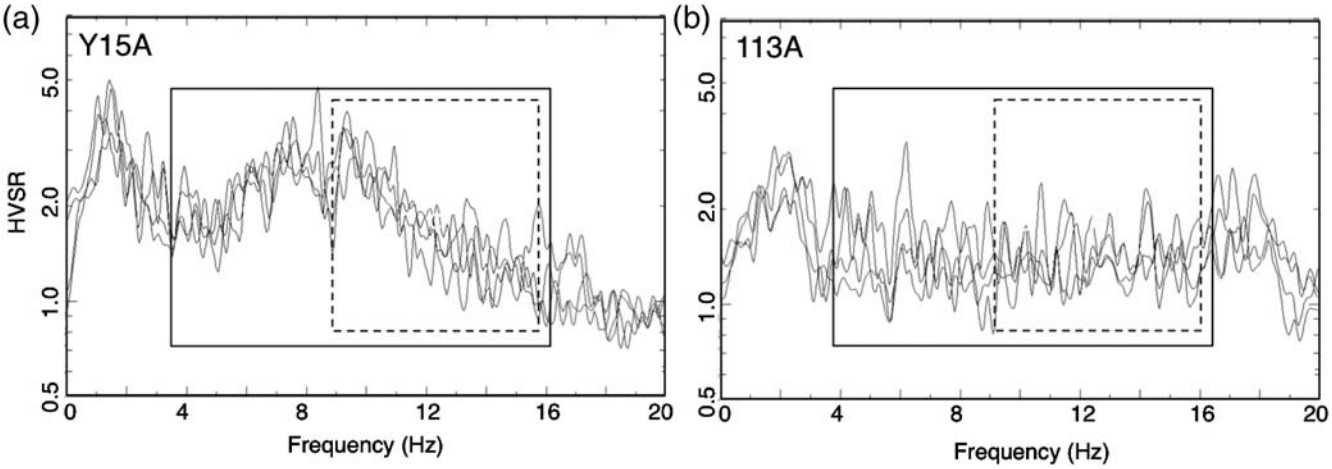

Figure 5. The mean horizontal-to-vertical spectral ratio (HVSR) (a) at site Y15A for 11 records, and (b) at 113A for 10 records. We show the mean for *S*-wave and coda windows, and for each horizontal component separately. At Y15A, there is a BB resonance peak, whereas at 113A no significant amplification is observed. The boxes indicate frequency ranges used to compute κ. Solid box represents within the bandwidth where we measure $\kappa_{r_{DS}}$ (4–16 Hz), the amplification shape may mask the decay of the FAS at site Y15A. Dashed box represents within the bandwidth where we measure $\kappa_{r_{AS}}$ (9–16 Hz), the amplification shape may bias $\kappa_{r_{AS}}$ high at Y15A.

f_c corresponding to a $\Delta\sigma < \Delta\sigma_{\min}$. This would allow one to use the traditional AS approach above 5 Hz. This would lead to negative $\kappa_{r_{AS}}$ values (gray circles in Fig. 6d), because the acceleration FAS actually increases above 5 Hz. We believe that $\Delta\sigma$ cannot be lower than $\Delta\sigma_{\min}$ and that for these small events ($\mathbf{M} < 2$), we assume f_c lies outside the usable frequency range. Figure 6d is an example of how assuming lower $\Delta\sigma$ can lead to bias in κ estimates.

In Figure 7a, we observe and compare $\kappa_{r_{AS}}$ estimates from the $\Delta\sigma_{\max}$ assumption (crosses) and $\kappa_{r_{DS}}$ from the $\Delta\sigma_{\min}$ assumption (circles) versus epicentral distance. $\kappa_{r_{DS}}$ does not increase with distance in the first 80 km, and its mean value out to that distance is $\kappa_{0_{DS}} = 0.050$ s (upper thin dashed line). Surprisingly, the two firmest rock sites, 113A and Y16A, have large $\kappa_{r_{DS}}$ values. But these data were recorded at long distances, and so the complex path attenuation pattern may obscure the site attenuation contribution in this limited bandwidth. Besides these two outliers, there is one more site with an unexpected value of $\kappa_{r_{DS}}$: the records at Y15A have a value of only 0.015 s at 120 km, perhaps due to site resonance, as previously discussed. Figure 5 shows that a BB resonance lies within the bandwidth where we measured $\kappa_{r_{DS}}$ (4–16 Hz) and may mask the FAS decay. For this reason, we do not include the $\kappa_{r_{DS}}$ value from this station when it comes to estimating our final model. Similarly to $\kappa_{r_{DS}}$, $\kappa_{r_{AS}}$ estimates close to the source do not increase with distance. Out to 50 km, the mean $\kappa_{0_{AS}}$ is about 0.017 s (lower thin dashed line). Comparing the two approaches, the DS approach yields higher κ than the AS. Within 60 km, this difference is about a factor of 3. Biasi and Anderson (2007) and Kilb *et al.* (2012) found a factor of 2 difference between κ values estimated using AS and DS. The larger factor we find here may be due to the magnitude range. We used **M** 1.2–1.5 for DS and **M** 3.1–3.4 for AS. Both these ranges fall within the range of **M** 1–3.5, in which Kilb *et al.* (2012) consider κ to be somewhat ill defined, because f_c falls in the range of frequencies used in the kappa measurements, making the results not optimal. We were forced to apply the DS approach to magnitudes above optimal ($\mathbf{M} < 1$) and the AS method to magnitudes below optimal ($\mathbf{M} > 3.5$). Another possible reason behind the discrepancy between AS and DS approach results (what we will call spectral droop) is mentioned later in the Discussion section.

Our goal is to estimate κ_0 in southern Arizona. As it is not possible to do this for each site individually, due to the paucity of data, we interpret all data of Figure 7a together to derive a model of κ_r with distance and a single value of κ_0, which we will consider as representative over the ensemble of sites in the region under study. Taking AS and DS results together, κ_r values remain constant at short distances from the source, and then begin to increase with distance. So we cannot assume an entirely linear relation of κ_r with distance and extrapolate to $R_e = 0$ to get κ_0. Instead, we propose a hockey-stick model, with constant κ_r out to a given distance, and then a linear increase with distance. We choose this reference distance at 70 km, because at longer distances the scatter in observations increases rapidly. Both the AS and DS approach close-by results contribute to the ensemble κ_0, whose mean value is 0.033 ± 0.014 s (thick dashed line).

For larger distances, the distance dependence (slope) will be determined by the AS approach, for which there are more distant records. $\kappa_{r_{AS}}$ generally increases above 70 km, as is commonly observed. Because of the large scatter, for simplicity we consider the increase linear (thick dashed line in Fig. 7a). From the slope of this line ($m = 0.00032$) and assuming a mean shear-wave velocity in the crust of $\beta =$ 3.5 km/s, we infer a mean *S*-wave *Q*-value of $Q = 1/\beta m =$ 900 for the region, which is frequency independent within

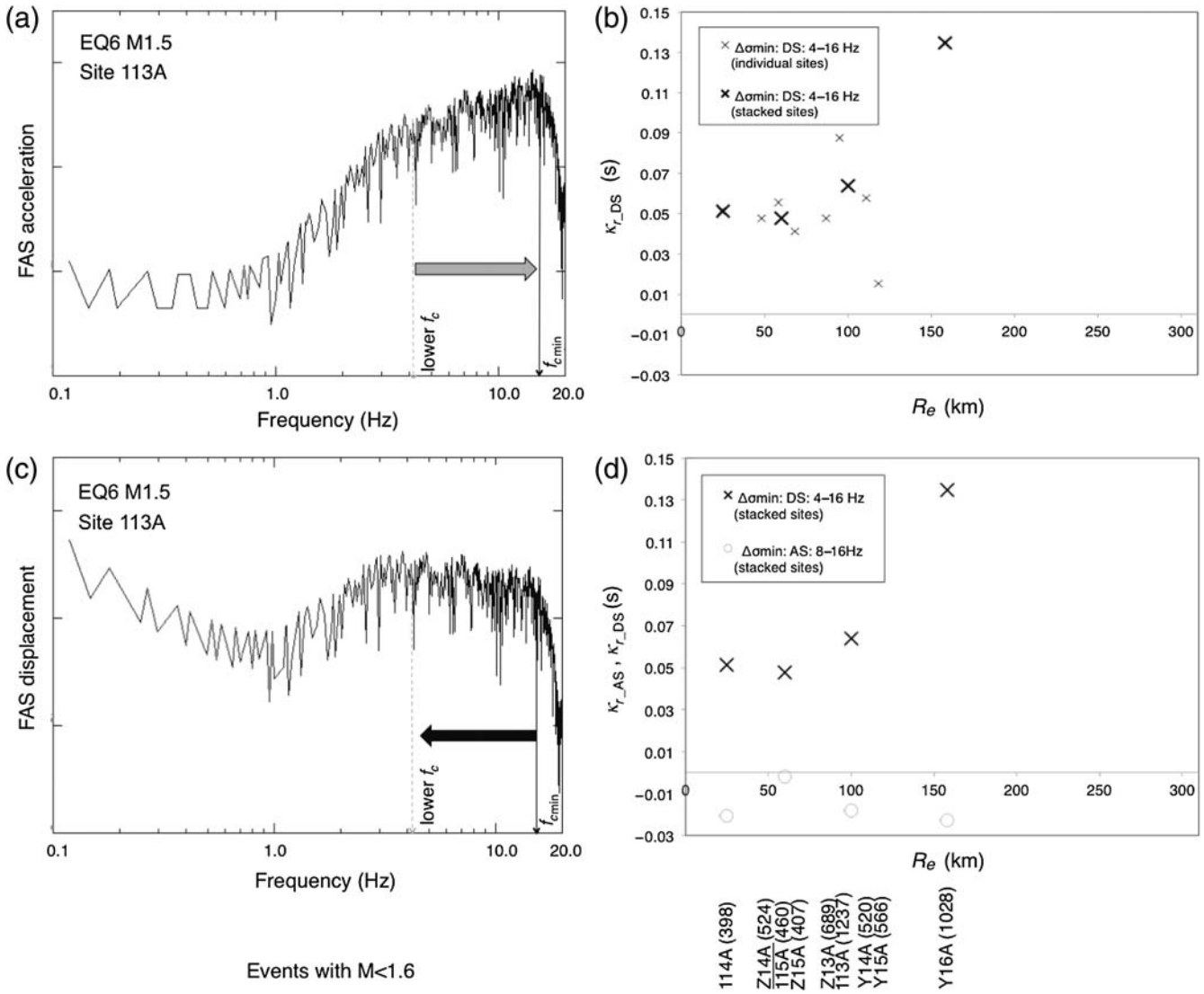

Figure 6. (a) An example of the acceleration FAS at site 113A for an **M** 1.5 event. (b) $\kappa_{r_{DS}}$ results versus distance for FAS stacked per site (small crosses) and FAS stacked per group of sites (large crosses), assuming $f_{c\,min}$. (c) Displacement FAS for the same record. Also marked, $f_{c\,min}$ and an even lower alternative f_c value that could interpret the break in the FAS. (d) Comparison of $\kappa_{r_{DS}}$ results for FAS stacked per group of sites assuming $f_{c\,min}$ (crosses) and $\kappa_{r_{AS}}$ results assuming the lower f_c (circles); the lower f_c assumption makes the κ values negative and is thus incorrect. Names and V_{S30} values of stations are also shown.

the bandwidth analyzed with the AS approach (9–16 Hz). Q may vary between 600 and 1300 (900 ± 300), a range that we estimate through a jackknife analysis and is shown in Figure 7a with a shaded area. In Figure 8, we show residuals for our model (i.e., for our κ_r estimates vs. the proposed model) with distance and V_{S30}. The residuals with distance are well balanced around 0, and there is no clear scaling of residuals with V_{S30}.

In Figure 7b, we compare our range of Q estimates with various regional Q estimates from the literature. For the Basin and Range including southern Arizona, Pasyanos (2013) estimated Q_S of 500–600 at 6–10 Hz. Assuming the dependence of Q with frequency at higher frequencies is also described by equation (7), and extrapolating their model to 16 Hz leads to a Q of 850. In Figure 7b, we illustrate this Q range as Pasyanos. In contrast, for the Colorado plateau (including northern Arizona), Pasyanos (2013) estimated Q in the 2000–5000 range for 6–12 Hz (which yields 6000 if we extrapolate to 16 Hz). Phillips *et al.* (2013) find Q_{Lg} between 500 and 1200 for 6–12 Hz (marked as Phillips range in the figure) for southern Arizona. In the area under study here, Phillips *et al.* (2013) find the Q structure to be rather complex, with large lateral variability. The heterogeneity along the paths that the rays follow between different sources and stations in this study can also explain the large scatter observed in κ_r measurements. Between 6 and 10 Hz, Beck *et al.* (2013) find Q_c to be 400–450 in the Basin and Range area and the transition zone, respectively; however, they have poor coverage in that region. Using the $Q(f)$ equations of Erikson *et al.* (2004) for the Basin and Range, we find Q_{Lg}

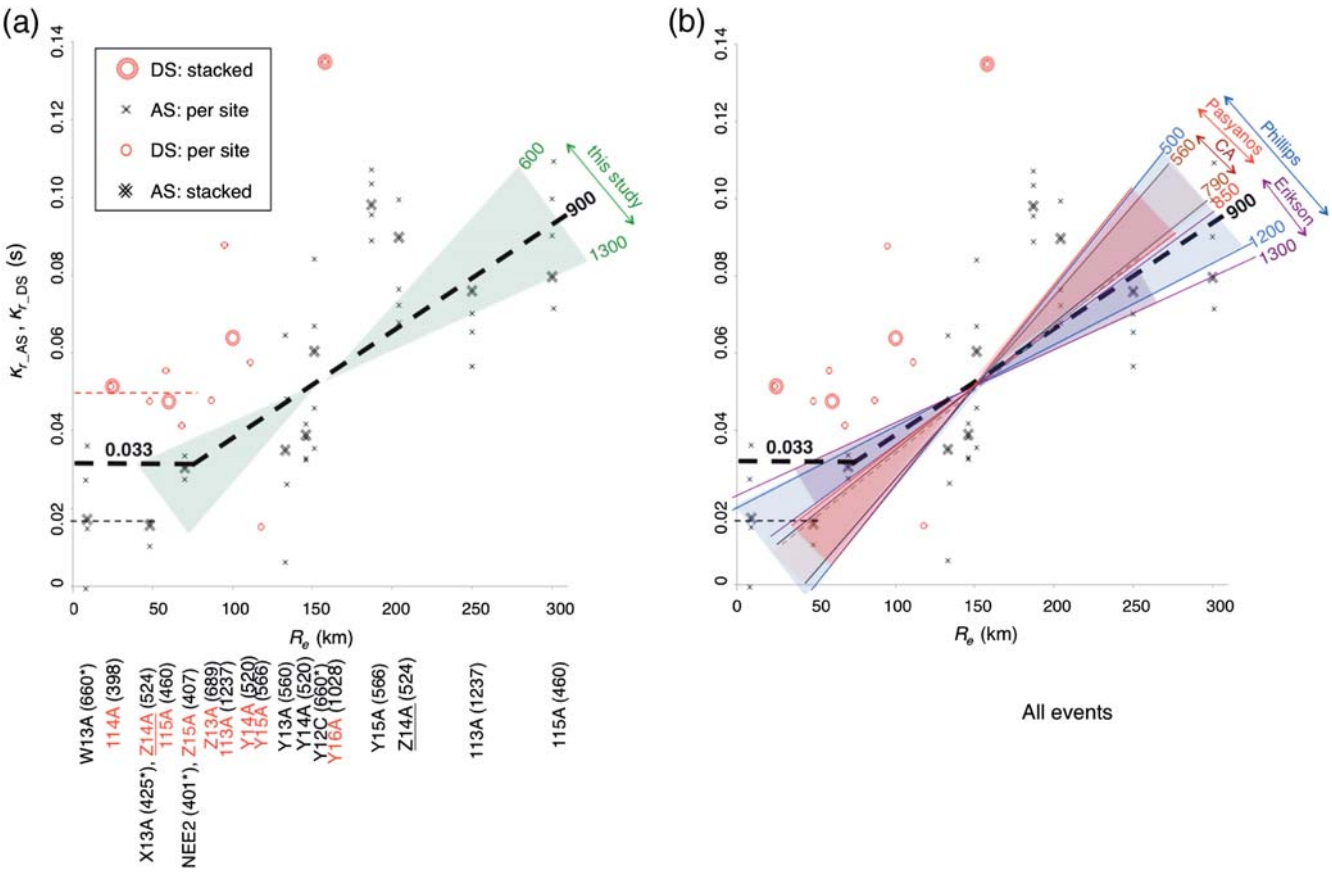

Figure 7. (a) All measured $\kappa_{r_{DS}}$ (circles) and $\kappa_{r_{AS}}$ (crosses) values versus epicentral distance. The final proposed model (thick dashed line) over all the sites studied has $\kappa_0 = 0.033 \pm 0.014$ s and $Q = 900 \pm 300$. The shaded zone shows possible Q values from regressions on subsets of our data points. Names and V_{S30} values of stations are also shown. (b) Comparison with Q models from the literature. Phillips range shows Arizona Q_{Lg} values of Phillips *et al.* (2013) for 6–12 Hz, Pasyanos range shows southern Arizona Q_S values from Pasyanos (2013) for 9–16 Hz, CA range shows typical California Q values for 9–16 Hz, and Erikson range shows the Erickson *et al.* (2004) Q_{Lg} values for the Basin and Range between 9 and 16 Hz. The color version of this figure is available only in the electronic edition.

between 875 and 1300 at 9–16 Hz (range shown in the figure as Erikson). The Q we infer from our data is within the range of the aforementioned estimates. Because the study region is also close to California, we also compare to a typical California Q model ($Q(f) = 150 \times f^{0.6}$; Silva *et al.*, 1997) at 9–16 Hz, which yields a Q range of 560–790 (shown in the figure as CA). Also, Erickson *et al.* (2004) find Q_{Lg} between 500 and 800 in California. These Q values for California are similar to what Pasyanos (2013) finds for southern Arizona. Erickson *et al.* (2004) and Beck *et al.* (2013) suggest that Q values for Arizona lie closer to California values than to typical CEUS. The Q inferred from our data is somewhat higher than California Q, but lower than CEUS estimates in agreement with Erickson *et al.* (2004).

We mentioned in the beginning that all FAS were first corrected for the class-specific, linear-elastic amplification functions of Figure 3c. We also checked the sensitivity of our model (the κ_0 and Q estimates) to the correction, that is, we test how important it is to make it. If we ignore the amplification, this produces lower κ estimates by about 35%: out to 70 km, the mean $\kappa_{0_{DS}}$ drops from 0.050 to 0.034 s; the mean $\kappa_{0_{AS}}$ drops from 0.017 to 0.011 s; and the ensemble mean κ_0 (from combining AS and DS approaches) drops from 0.033 to 0.021 s. We stress again that this is because the transfer function is not flat within the frequency range where $\kappa_{r_{AS}}$ and $\kappa_{r_{AS}}$ are estimated. In contrast, the effect of the amplification correction on the estimate of Q by the AS approach is minimal, as the slope is not affected if all the $\kappa_{r_{AS}}$ values that define it drop by the same amount. We conclude that amplification can have a significant effect on κ_0 when using the AS and DS approaches, depending on the frequency range used. As most studies do not correct for crustal amplification, we consider this an important result.

BB Approach

The parameters in equation (3), which are inverted, are $\kappa_{0_{BB}}$, $\Delta\sigma(f_c)$, and M_w. We use FAS from 14 sites. Because of the insufficient distance range and bandwidth, we fix $Q(f)$ and R_C. We constrained $Q(f)$ to be $200 \times f^{0.68}$ from the Erickson *et al.* (2004) model for the Basin and Range (which is also similar to Beck *et al.*, 2013; Pasyanos, 2013; Phillips *et al.*, 2013). This $Q(f)$ model is consistent with geometrical

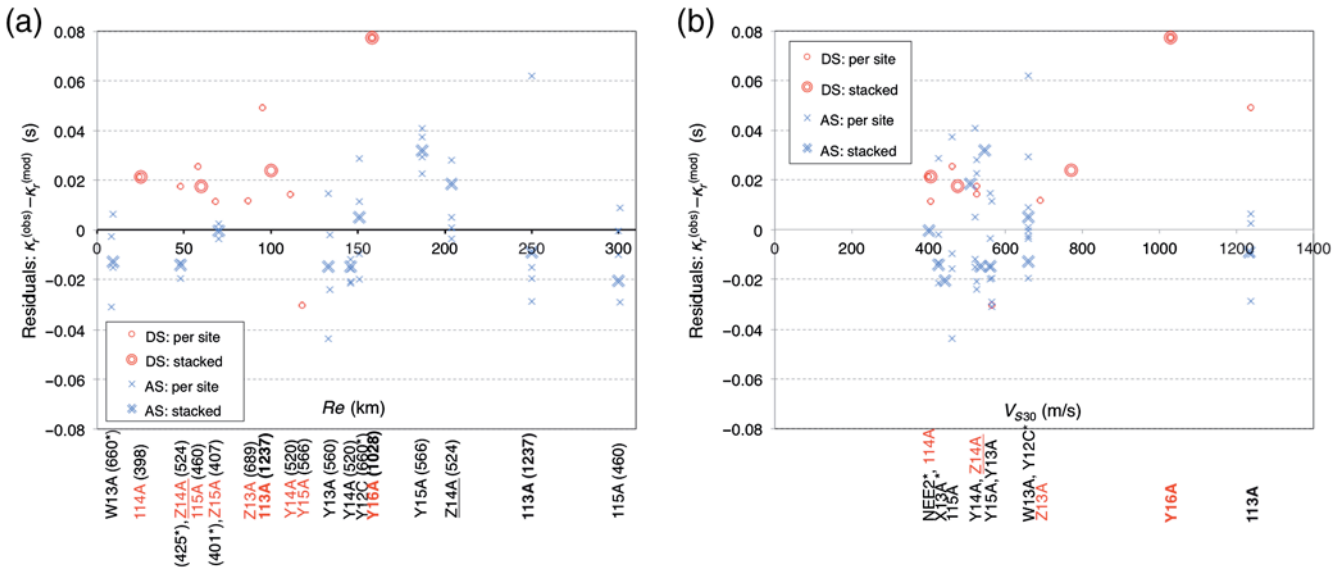

Figure 8. Residuals of all measured $\kappa_{r_{DS}}$ (circles) and $\kappa_{r_{AS}}$ (crosses) values with respect to the final proposed model versus (a) epicentral distance and (b) V_{S30}. Names of stations and their respective V_{S30} values are listed in the x axis. The color version of this figure is available only in the electronic edition.

spreading of $1/R^{0.5}$ for that province. R_C was fixed at 40 km, based on initial inversions that had a starting value of 80 km. Table 4 lists the initial values assumed for the model parameters (mean $\kappa_{0_{BB}}$ and initial reported **M** converted to M_w). Initial κ_0 was taken at 0.04 s, a typical value for stiff sites in WUS. It was assumed that for the source region shear-wave velocity is 3.5 km/s and density is 2.75 cgs (typical WUS values at 8 km depth). When it came to $\Delta\sigma$, we were guided by the study of Silva and Darragh (2014) in Washington, which also used TA data. In that study, the inversion converged in two ways: either assuming $f_c < 16$ Hz with a very low $\Delta\sigma$ value (< 1 bar), or by fixing f_c beyond 16 Hz and assuming that $\Delta\sigma$ could not be resolved within the 16 Hz limit of the TA data. Similarly, for the small Arizona events (**M** < 1.6) in this study, we fixed f_c beyond 16 Hz. Initial $\Delta\sigma$ was thus taken at 5 bars, a typical value for small events in WUS that yields f_c outside our bandwidth.

Figure 9 shows the recorded FAS and the initial and final models per site for two events: the largest (**M** 3.4) and one of the smallest (**M** 1.5). For the larger event (Fig. 9a), the plateau and the beginning of the high-frequency decay are visible; more so for more distant sites, where path attenuation adds to site attenuation. For the smaller event (Fig. 9b), there is no sign of the decay, and the FAS continues to rise at all sites without reaching the f_c, even for distant sites.

To assess the stability of the median $\kappa_{0_{BB}}$, we made a suite of inversions where $Q(f)$ models and crustal amplification were modified. The four models are:

1. fixed $Q(f)$ to the Erickson *et al.* (2004) model,
2. fixed $Q(f)$ to a southern California model (because our region is adjacent to it),
3. fixed $Q(f)$ to a frequency-independent value of 1000 ($\eta = 0$, similar to the Q model from the AS approach),
4. fixed $Q(f)$ to the Erickson *et al.* (2004) model and fixed all transfer functions to unity (ignored amplification correction).

Table 4 lists the parameters for the four models, namely Q_0, η, median $\kappa_{0_{BB}}$ over the ensemble of sites, the mean **M**, and the mean/median ratio computed for the fit of the model to the FAS (this constitutes a goodness-of-fit index). The $\Delta\sigma$ values are not shown, as they are not reliable due to the combination of limited bandwidth and small magnitudes used in the inversion. Furthermore, the narrow bandwidth

Table 4
Broadband Inversion Results per Model

	Q	η	$\bar{\kappa}_{0_{BB}}$ (s)	$\bar{\mathbf{M}}$	Mean/Median	Amplification
Starting model	200	0.68	0.040	1.97	1.56	Rock/soil
Model 1	200*	0.68*	0.033	2.14	1.13	Rock/soil
Model 2	152*	0.72*	0.034	2.17	1.16	Rock/soil
Model 3	1000*	0.00*	0.024	2.00	1.12	Rock/soil
Model 4	200*	0.68*	0.034	2.37	1.15	Unity

*Fixed parameters, R_c fixed at 40 km.

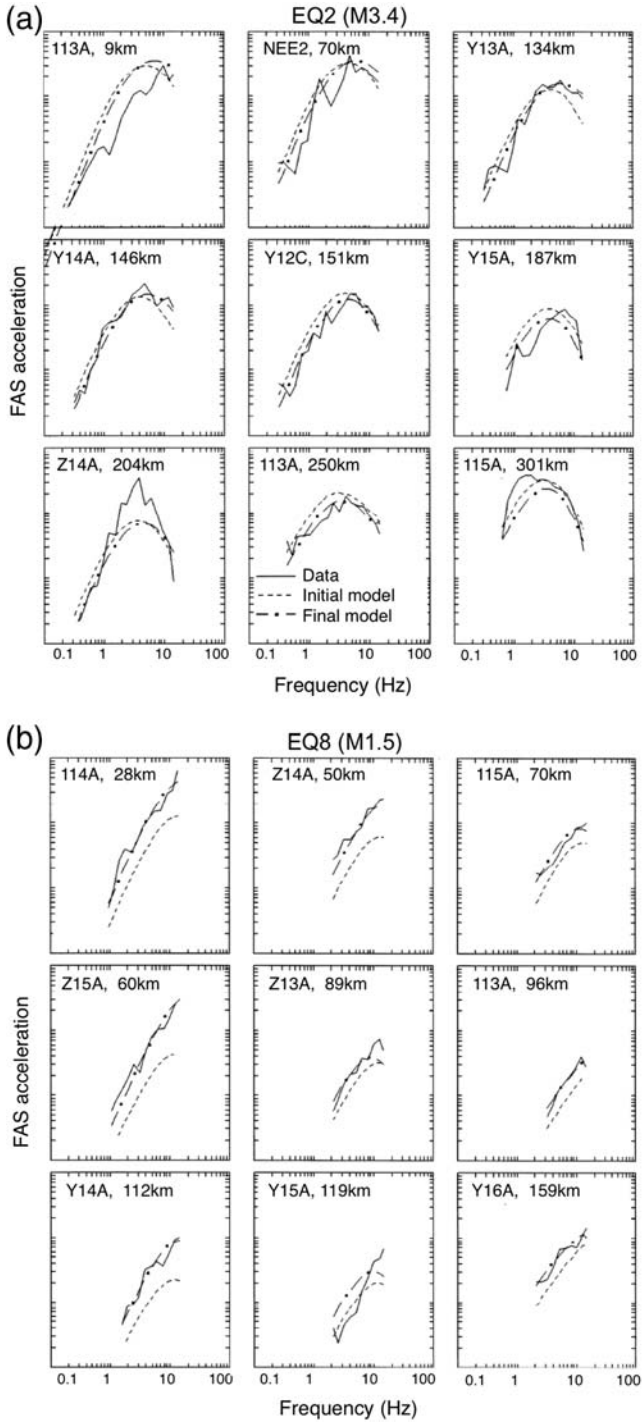

Figure 9. (a) Comparison of the model 1 BB (initial and final) models with the recorded FAS at all sites that recorded EQ2 (**M** 3.4). (b) Same as (a), for EQ8 (**M** 1.5).

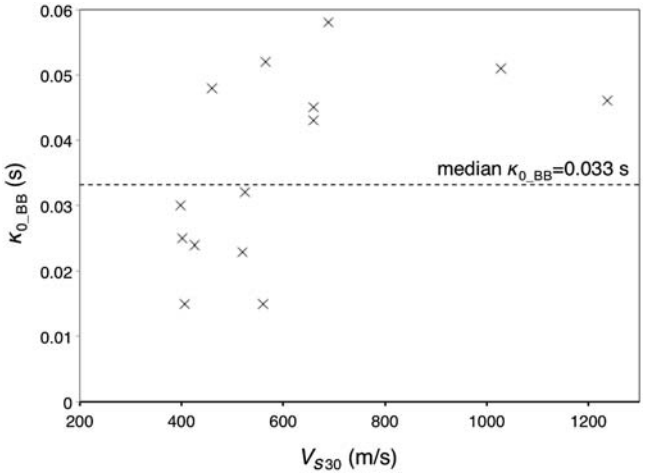

Figure 10. $\kappa_{0_{BB}}$ estimates for individual stations versus V_{S30} (dashed line shows the median value of 0.033 s).

and lack of near-field records are likely to cause coupling between individual $\kappa_{0_{BB}}$ values at different sites. Hence, we consider the median κ value more robust than the individual ones (e.g., see Table 5 and Fig. 10 for model 1). The best estimate for the median $\kappa_{0_{BB}}$, the mean M_w, and the mean/median ratio is given by model 1. In model 2, shifting from Arizona $Q(f)$ to southern California $Q(f)$ does not affect the median $\kappa_{0_{BB}}$. In model 3, shifting to a frequency-independent Q model decreases the median $\kappa_{0_{BB}}$ to 0.024 s (about 40%). Finally, in model 4, shifting from the (correct) crustal amplification to unity amplification does not affect the median $\kappa_{0_{BB}}$. However, in model 4 the shift in amplitude is now accommodated by a significant increase in mean **M**, showing the trade-off between the parameters (see, also, the next paragraph). In contrast, in the Combining the AS and DS Approach section, a change in amplification had a very strong effect on κ in the AS and DS approaches.

We also make a sensitivity check: by varying the value of each parameter in the initial model by a given amount, we estimate the impact on the resulting $\kappa_{0_{BB}}$ and assess epistemic uncertainty. We varied Q_0, η, and R_C by $\pm 50\%$, which we consider a realistic estimate of variability for those parameters, and we varied $\Delta\sigma$ and κ_0 by $\pm 100\%$, as these two are more variable. In Table 6, we show how changes in the model parameters affect the median $\kappa_{0_{BB}}$. All other inversion parameters, such as M_w and $\Delta\sigma$, change along with $\kappa_{0_{BB}}$. $\kappa_{0_{BB}}$ is mostly coupled with η, and reducing the latter by 50% causes a reduction of 30% in the former. Hence, the $\kappa_{0_{BB}}$ values computed should be regarded as contingent to the particular $Q(f)$ and R_C values assumed. Taking each parameter independently and varying it by a realistic amount leads to uncertainty in the median $\kappa_{0_{BB}}$ of at least $\sigma_\mu = 0.3(\ln)$. If we also consider the coupling between Q_0, η, and κ in this dataset, we suggest increasing the epistemic uncertainty in the median $\kappa_{0_{BB}}$ to 0.5 (ln). As $\kappa_{0_{BB}}$ values for individual stations are highly correlated (80%), for individual site $\kappa_{0_{BB}}$ values we suggest a maximum uncertainty of 0.6 (ln).

One final effort to estimate the epistemic uncertainty (as there were not enough data to implement a jackknife approach) was to investigate the effect of smoothing of the FAS on $\kappa_{0_{BB}}$. In the previous analyses, FAS were smoothed on a logarithmic scale for an equal number of points across all frequencies. We repeated the analysis for linear smoothing, which yields an increased number of points at high

Table 5
$\kappa_{0_{BB}}$ Results per Site from Inversion Using Model 1

Site	$\kappa_{0_{BB}}$ (s)
113A	0.046
114A	0.030
115A	0.048
Y14A	0.023
Y15A	0.052
Z13A	0.058
Z14A	0.032
Z15A	0.015
NEE2	0.025
W13A	0.045
X13A	0.024
Y13A	0.015
Y12C	0.043
Y16A	0.051
Median	0.033

Table 6
Effect on Median $\kappa_{0_{BB}}$ from Variations in the Inversion Input Parameters

Parameter Variations	Change in Median $\kappa_{0_{BB}}$ (s)
$Q_0/1.5$	$\kappa/1.14$
$Q_0 \times 1.5$	$\kappa \times 1.03$
$\eta/1.5$	$\kappa/1.32$
$\eta \times 1.5$	$\kappa \times 1.21$
$R_C/1.5$	$\kappa \times 1.02$
$R_C \times 1.5$	$\kappa \times 1.03$
$\kappa/2$	$\kappa \times 1.01$
$\kappa \times 2$	$\kappa \times 1.01$
$\Delta\sigma \times 2$	$\kappa \times 1.09$
$\Delta\sigma/2$	$\kappa/1.06$
No amplification*	$\kappa \times 1.03$

*Replaced rock and soil transfer functions with unity.

frequencies and thus weighs them more, emphasizing $\Delta\sigma$, κ_0, and $Q(f)$ at longer distances, rather than magnitude. Assigning more weight to high frequencies for large events will tend to emphasize the frequency range in which the point-source stochastic model (PSSM) works best, and focus less on the range where its performance is not as good. Assigning equal weight across the entire inversion bandwidth is better suited for small events, where the PSSM seems to work equally well at high and low frequencies. Our sensitivity check shows that the effect of smoothing on the median $\kappa_{0_{BB}}$ is of the order of 10%, which is small compared to the epistemic uncertainty in Table 6.

As found in the AS and DS approach, individual site $\kappa_{0_{BB}}$ estimates show little dependence on V_{S30} (Fig. 10). The two stiffest sites have κ_0 estimates of 0.046 and 0.051 s, possibly because regional $Q(f)$ again overwhelmed a small κ_0 value. Overall, for the BB approach, the best estimate of κ_0 across the ensemble of sites is the median of model 1: $\kappa_{0_{BB}} = 0.033$ s with an uncertainty of 0.6 (ln).

Discussion

Model Comparison

The results of all approaches are summarized in Figure 11. The first κ model combines the bandlimited AS (assuming $\Delta\sigma_{max}$) and DS approaches (assuming $\Delta\sigma_{min}$), using events above **M** 3 and below **M** 1.6, respectively. Over the 8–16 Hz frequency range, this yielded a mean $\kappa_0 = 0.033 \pm 0.014$ s (i.e., 0.019–0.047 s), and a mean frequency-independent regional Q of 900 ± 300. Within the first 50 km, the DS method (rendered more robust through stacking) yielded κ estimates larger than the AS by a factor of 3. The second κ model is derived from the BB approach, using all events, and fixing $Q(f)$ and R_C. Models 1, 2, and 4 yield practically the same median κ_0 of 0.033 s, and a Q range of 850–1050 at 8–16 Hz. Based on realistic variations of the model parameters, the uncertainty of this median is 0.5 (ln), that is, from 0.020 to 0.054 s. Model 3 assuming constant Q produced a κ_0 of 0.024 s, which is within this range of uncertainty.

Both approaches lead to similar findings: (1) the best estimate of κ_0 is the mean over the ensemble of stations, and there is no correlation between individual station κ_0 values and station stiffness (the two hardest stations had some of the highest κ values); (2) this mean κ_0 is practically the same for both approaches, as is its range; (3) the resulting Q ranges are consistent, between approaches, and within the (large) scatter of independent estimates for the region; (4) both approaches infer stress drops higher than those estimated by Phillips *et al.* (2013); for the smallest earthquakes, we infer f_c values above our bandwidth.

The two approaches (AS/DS and BB) have different sensitivities to (1) crustal amplification: correcting the FAS decreased κ_0 in the AS/DS approach by 35%, whereas in the BB approach it primarily changed the estimate of M_w. (2) $Q(f)$ models: in the BB approach, κ_0 did not change significantly when Q_0 and η varied, but a constant-Q model reduced it by 40%. In the AS/DS approach, the hockey-stick model helps constrain κ_0 using nearby records, reducing sensitivity to the slope (Q).

Engineering Application: Effects of Our Results on GMPE Adjustments

One use of the region-specific κ_0 values is to adjust global GMPEs (such as the NGA-West2 models) from a host region, where the models were developed using data, to a specific target region, poor in data, where an empirical GMPE cannot be derived. This can be done, for example, using the hybrid empirical approach (Campbell, 2003, 2004) or the inverse random vibration theory (IRVT) approach of Al Atik *et al.* (2013) and accounting for differences between seismological parameters in the host and target region, including differences in κ_0. In the IRVT approach, the host κ_0 (i.e., the native κ_0 of the GMPE) is estimated based on response spectra that are generated from the GMPE for a suite of magnitude and distance

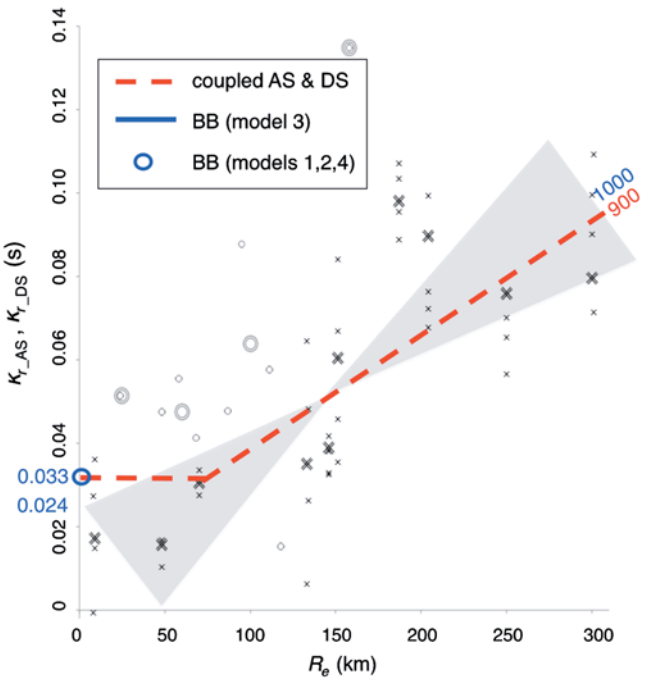

Figure 11. Comparison of results from the different methods applied: coupled AS and DS approaches (thick dashed line), model 3 of the BB approach (thick solid line, constant Q of 1000, $\kappa_{0_{BB}} = 0.024s$), and models 1, 2, and 4 of the BB approach ($\kappa_{0_{BB}} = 0.033$ s). Gray range shows the different Q models found in the literature. The color version of this figure is available only in the electronic edition.

scenarios, which are then inverted into FAS. On these FAS, the host $\kappa_{0_{IRVT}}$ can be estimated in the traditional way, as in the AS approach, off the high-frequency slope, and averaged for the different scenarios. Similarly, to adjust these FAS to a different target κ_0, the high-frequency slope is modified accordingly. The corrected FAS can then be converted into response spectra again.

The estimated κ_0 values for southern Arizona from this study are centered at 0.033 s (0.020–0.054 s range). GeoPantech (2015) estimated the host κ_0 values for the NGA-West2 GMPEs for a reference V_{S30} of 760 m/s using the IRVT approach. They found a median host κ_0 of 0.040 s (0.036–0.044 s range) in the 5–20 Hz frequency range, where the maximum spectral decay is observed, and 0.033 s (0.031–0.035 s) in the 5–30 Hz range. The values computed for each of the four GMPEs used are shown in Table 7. In chapter 3, Darragh *et al.* (PEER, 2015) estimated the host κ_0 values using the BB inversion approach described in this article. They used a frequency range up to 30 Hz and estimated a mean host κ_0 value of 0.030 s. This is consistent with the latter result of the IRVT approach. Although southern Arizona is a significantly less active region than California (for which we might expect significantly lower κ_0 values), the range of the region-specific κ_0 estimates we found in this study are consistent with the host κ_0 values estimated for the BB approach, and only slightly lower than the host κ_0 values estimated for the IRVT approach. Thus, given the uncertainties

Table 7
Host κ_0 Values for Next Generation Attenuation-West 2 Project Ground-Motion Prediction Equations (GMPEs) Based on the Inverse Random Vibration Theory (IRVT) Approach

GMPE	$\kappa_{0_{IRVT}}$ (s): 5–20 Hz	$\kappa_{0_{IRVT}}$ (s): 5–30 Hz
Abrahamson *et al.* (2014)	0.045	0.033
Boore *et al.* (2014)	0.038	0.031
Campbell and Bozorgnia (2014)	0.037	0.033
Chiou and Youngs (2014)	0.041	0.035
Average	0.040	0.033

in the κ_0 estimates, we judge that the NGA-West2 GMPEs do not need to be adjusted for κ_0 differences for application to southern Arizona.

On the Applicability and Bias of the DS Approach

Unlike the AS approach, which has been used most often in the literature, the DS approach has seen very few applications, and in these it has often been coupled with AS (e.g., Kilb *et al.*, 2012). One of its advantages over the AS is that if the ω^{-2} assumption breaks down (e.g., in the case of ω^{-3} FAS for small events, which we did not examine in this study and is hence one of its limitations), it may affect $\kappa_{r_{AS}}$ estimates but not so much $\kappa_{r_{DS}}$ estimates, as the latter are measured where the FAS is really flat. On the other hand, before DS can entirely and reliably substitute for AS in the future (thus necessitating only very small events to characterize site attenuation), one issue that needs to be investigated further is the systematic discrepancy between the two approaches. This discrepancy is currently within a factor of 2–3. In this section, we perform a preliminary test to investigate the effect of f_c on $\kappa_{r_{DS}}$ and a possible reason for the DS versus AS discrepancy.

Let us assume a displacement FAS not affected by any site or path attenuation (no κ_0 or Q terms), and let us focus only on the shape of the FAS due to the f_c. The shape will be given by the formula

$$d = \frac{1}{f^2 + f_c^2} = \frac{1/f^2}{1 + f^2/f_c^2} = \frac{C}{1 + f^2/f_c^2}. \qquad (8)$$

This equation implies that, at low frequencies, the spectrum is horizontal only as long as the frequencies are significantly lower than f_c. For instance, at $f = 0$, $d = $ C. As frequency f increases, d decreases. At $f = 0.5f_c$, $d = 0.8C$. As f approaches the value of f_c, the spectral value d begins to decrease faster, and at $f = f_c$, $d = 0.5C$, that is, half of its low-frequency asymptotic value. This slope in the spectral shape, observed without accounting for any path or site attenuation, due merely to the vicinity of f_c, will affect any estimates of κ_{DS} attempted over frequency bands close to f_c. For instance, if κ_{DS} is measured right below f_c ($d = 0.5C$), it will be strongly affected, whereas if it is mea-

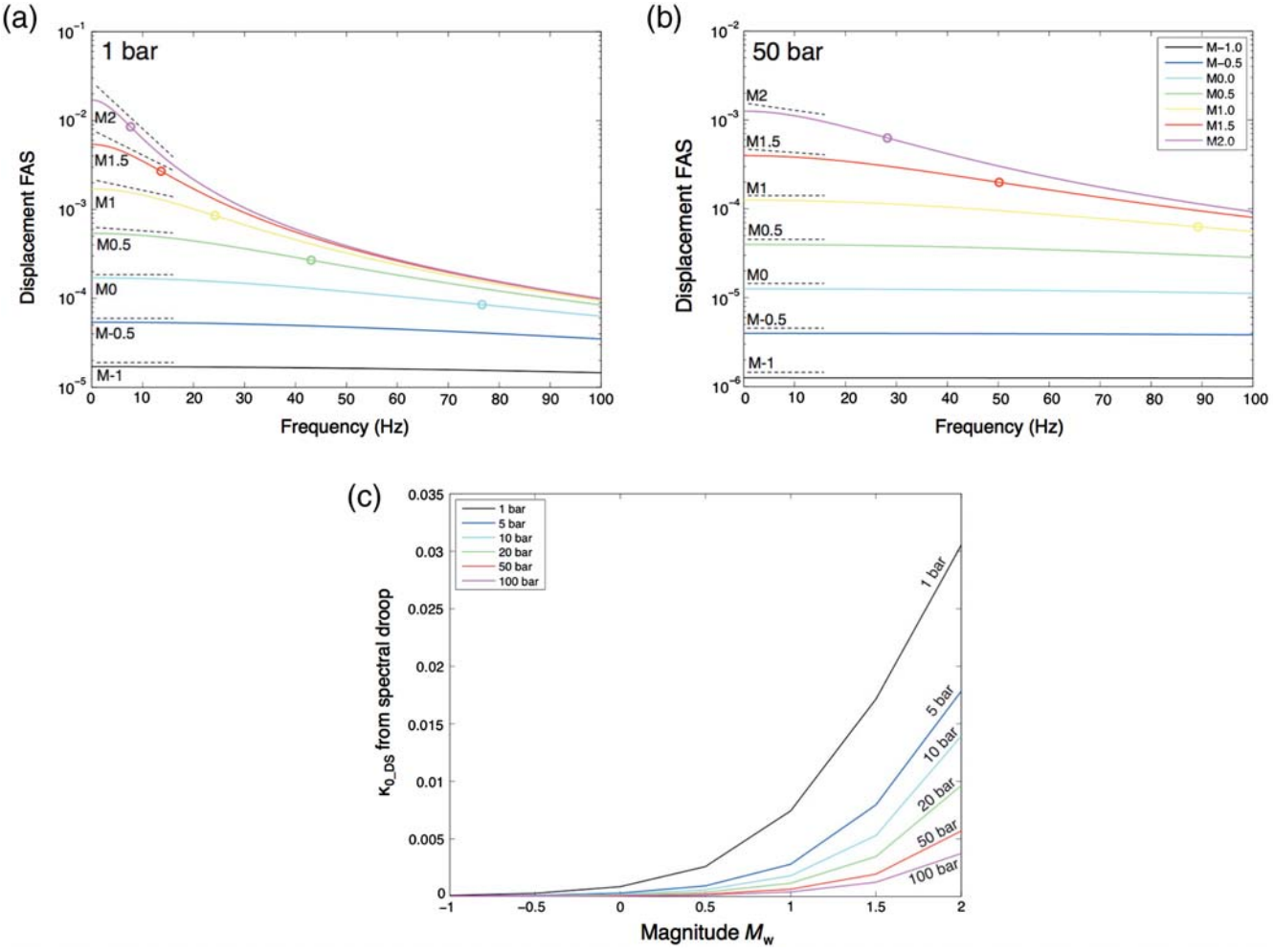

Figure 12. (a) Example shape of displacement FAS for 1 bar, based only on f_c and excluding site and path attenuation. Circles indicate f_c. The slopes of the short lines are proportional to the overestimates in $\kappa_{0_{DS}}$ caused by the mathematical shapes of the respective DS (equation 8). (b) Same as (a), for 50 bar. (c) Apparent $\kappa_{0_{DS}}$ (bias) per magnitude due to the effect of f_c (spectral droop) for different stress-drop values. We assume lowest useable frequency (LUF) = 0 and highest usable frequency (HUF) = 16 Hz, to mimic Transportable Array (TA) band limitation. The color version of this figure is available only in the electronic edition.

sured, say, below $0.5f_c$ ($d = 0.8C$), the effect will be much smaller. We will call this bias due to f_c spectral droop or apparent κ (G. Biasi, personal comm., 2016) and will assume that for practical purposes, the effect on κ is low enough below $0.5f_c$.

Figure 12a,b illustrates the f_c effects through example FAS shapes for a large range of magnitudes (**M** − 2 to 2), for the two limit cases of stress drop of this study, $\Delta\sigma_{\min}$ (1 bar) and $\Delta\sigma_{\min}$ (50 bar). We plot the shape up to 100 Hz for illustrative purposes; when using data we know that the bandwidth is much more limited. The circular markers indicate f_c per magnitude. In the vicinity of f_c, the spectral droop can be observed. The droop is more pronounced for larger magnitudes, where f_c is lower. The slopes of the short lines in the figure are proportional to the overestimates in $\kappa_{0_{DS}}$ caused by the f_c effect. We also note that the lower the $\Delta\sigma$, the stronger the droop effect, because we do not have enough bandwidth below f_c to move below $0.5f_c$. We calculate the slope of the FAS shape for each case between 0 and 16 Hz (roughly the range used for κ in this study, keeping HUF = 16 Hz to simulate the TA band limitation), and from that we compute the apparent κ. Because this is distance independent, the notion directly applies to κ_0 as well. Apparent κ values are shown in Figure 12c for different magnitude and stress-drop pairs. Below **M** − 1, f_c is too high to affect κ (HUF $\ll 0.5f_c$). Above **M** 0, the effect of f_c translates into a positive κ, that is, an overestimation of $\kappa_{r_{DS}}$ that is added to the actual attenuation when measuring close to f_c. The lower the $\Delta\sigma$, the stronger the droop effect. At **M** 1.0, for 1 bar, $0.5f_c \sim 12$ Hz < HUF, and the overestimation is 0.008 s; for 50 bar, $0.5f_c \sim 44$ Hz ≫ HUF, and the overestimation is only 0.001 s. At **M** 1.5, for 1 bar, $0.5f_c \sim 7$ Hz < HUF, and the overestimation of 0.017 s is significant; for 50 bar, $0.5f_c \sim 25$ Hz > HUF, and the overestimation is only 0.002 s. So using an **M** 1.5 as we did here may be marginally acceptable for 50 bar, but could overestimate

κ_0 by as much as 20–30 ms for 1 bar. To be sure we are working below $0.5f_c$ (for HUF = 16 Hz in the TA), we need $f_c > 32$ Hz. For 1 bar, this means $\mathbf{M} < 0.8$, and for 50 bar it means $\mathbf{M} < 1.9$.

We should note here that, similar to the effect the f_c has on κ_{DS} when HUF nears it from below, it will have an effect on κ_{AS}, when LUF nears it from above; that is, the droop observed right below f_c on the displacement FAS will also be observed right above f_c on the acceleration FAS. Also in a similar manner, we can define a rule of thumb similar to HUF $> 0.5f_c$; this could be LUF $< 0.5f_c$. For our data, as seen in Figure 2b, LUF < 1 Hz for all records used in the AS method (i.e., events with $\mathbf{M} > 3$). From the same figure, we can see that regardless of stress-drop assumption, LUF values are less than $0.5f_c$. We can infer for our data that the f_c effect on κ_{AS}, that is, the value of apparent κ_{AS}, can be ignored. However, in the general case, we propose that it should also be considered, and that the effect of droop is generally not restricted to the DS approach but to both DS and AS.

We have not computed a value of $\Delta\sigma$ for our dataset, but we believe it lies closer to 50 bar than to 1 bar. For a possible range for stress drops of 5–50 bar, the possible errors in our $\kappa_{r_{\mathrm{DS}}}$ are likely below 0.007 s. The errors in $\kappa_{r_{\mathrm{AS}}}$ can be ignored. The expected discrepancy between AS and DS due to droop is about 0.007 s. This is small compared to the discrepancy we found between DS and AS approaches at short distances (0.050 vs. 0.017 s). Thus, we believe that the spectral droop (or apparent κ due to f_c) is only part of the reason behind this systematic discrepancy. The bias in the κ values shown in Figure 12c can be used as lower bounds to quantify the expected bias between DS and AS results (at any distance, because this is basically an additional term in the summation of site and path κ components) due to spectral droop. Other mechanisms should likely be considered to fully explain the discrepancy.

Conclusions

The TA has significantly added to the ground-motion data available for the United States. For low-seismicity regions, it often yields the vast majority of short-distance records. For critical structures in regions of sparse seismicity, it is important to estimate region-specific seismic hazard with whatever sparse data are available. In this context, this study proposes a framework for resolving κ_0 using bandlimited data such as the TA data in regions of low seismicity. We use a combination of the AS, DS, and BB approaches to overcome the various data limitations and address uncertainties. We propose a scheme where we do not have to resolve stress drop but only estimate lower and upper regional bounds for it.

κ_0 for southern Arizona based on the bandlimited (AS/DS) and the BB approach are similar in terms of mean (0.033 s) and range (0.5 in ln), and Q estimates (900 ± 300 at 9–16 Hz) are compatible between approaches and with literature. This κ_0 is similar to what is estimated for the NGA-West2 GMPEs, so these models can be used for southern Arizona without a κ_0 adjustment. When looking at individual stations, no clear correlation is found between individual site κ_0 values and site stiffness. We show the potential bias on κ_0—in conjunction with the frequency band used to estimate it—from not addressing crustal amplification. We propose one reason behind the known discrepancy between DS and AS estimates that is related to the bias (droop) due to the corner frequency when using DS (and, in the general case, also AS). Our analyses indicate that the stress drop in this region may be higher than what was found in other studies using TA data. This is likely due to the possibility of $f_{\max}$ (Hanks, 1982) masking the true source f_c, as was observed by Frankel (1982) for small earthquakes, and leading to smaller apparent f_c and hence stress drops.

The large range of κ_0 means the within-approach uncertainty is much larger than the between-approach uncertainty, and it cannot be reduced if the data quality is not improved. Frequency band limitation of the TA data is the largest obstacle for estimating κ and will remain a limiting factor for other locations that depend on the TA for short- and intermediate-distance records. Increasing the sampling rate of the seismic arrays that are deployed in these regions can greatly contribute toward avoiding such issues in the future.

Data and Resources

Ground-motion data for the Transportable Array (TA) can be downloaded from the Incorporated Research Institutions for Seismology (IRIS) website http://ds.iris.edu/ds/nodes/dmc/earthscope/usarray/ (last accessed September 2015). Information on the USArray can be found at http://www.usarray.org/researchers/obs/transportable (last accessed September 2015). For signal processing, we made use of SAC2008 (Goldstein *et al.*, 2003; http://www.iris.edu/software/sac; last accessed September 2015). Some figures were made using Generic Mapping Tools v.3.4 (Wessel and Smith, 1998; www.soest.hawaii.edu/gmt; last accessed September 2015). More information on the Southwestern United States Ground Motion Characterization (SWUS GMC) Senior Seismic Hazard Analysis Committee (SSHAC) Level 3 project can be found at www.pge.com/dcpp-ltsp/ (last accessed November 2016) and complete documentation is available in GeoPantech (2015).

Acknowledgments

This article is dedicated to the memory of Stephen P. Ktenides (1926–2016).

Many thanks go to Carola Di Alessandro and the Southwestern United States Ground Motion Characterization (SWUS GMC) project scientific partners for discussions and feedback. We thank an anonymous reviewer and Glenn Biasi for their thorough reviews of the article. We are also most grateful to Glenn for generously sharing his ideas on defining the most conservative frequency range and on the effect of spectral droop. The data collection, processing, site spectral analysis of surface waves characterization, and analyses were funded by the Pacific Earthquake Engineering Re-

search Center (PEER) and the SWUS GMC SSHAC Level 3 Project with the participation of Pacific Gas and Electric Company, Arizona Public Service, and partial participation of Southern California Edison. The first author was also funded by the French project SeIsmic Ground-Motion Assessment (SIGMA) and Pacific Gas and Electric Company, and the work presented here began when she was a visiting scholar at PEER.

References

Abrahamson, N. A., W. J. Silva, and R. Kamai (2014). Summary of the ASK14 ground motion relation for active crustal regions, *Earthq. Spectra* **30,** 1025–1055.

Aki, K. (1967). Scaling law of seismic spectrum, *J. Geophys. Res.* **72,** 1217–1231.

Al Atik, L., A. Kottke, N. A Abrahamson, and J. Hollenback (2013). Kappa (κ) scaling of ground motion prediction equations using an inverse random vibration theory approach, *Bull. Seismol. Soc. Am.* **14,** 336–346.

Ancheta, T. D., R. B. Darragh, J. P. Stewart, E. Seyhan, W. J. Silva, B. S. J. Chiou, K. E. Woodell, R. W. Graves, A. R. Kottke, D. M. Boore, *et al.* (2013). PEER NGA-West2 database, *PEER Report 2013/03, Pac. Earthq. Eng. Res. Ctr*, Berkeley, California.

Anderson, J. G., and S. E. Hough (1984). A model for the shape of the Fourier amplitude spectrum of acceleration at high frequencies, *Bull. Seismol. Soc. Am.* **74,** 1969–1993.

Anderson, J. G., and J. R. Humphrey (1991). A least squares method for objective determination of earthquake source parameters, *Seismol. Res. Lett.* **62,** 201–209.

Atkinson, G. M., and W. Silva (1997). An empirical study of earthquake source spectra for California earthquakes, *Bull. Seismol. Soc. Am.* **87,** 97–113.

Beck, S., L. Linkimer, G. Zandt, and A. Holland (2013). Focal mechanisms and preliminary attenuation measurements in Arizona, *Report CR-13-C*, Arizona Geological Survey, 24 pp., available at repository.azgs.az.gov/sites/default/files/dlio/files/nid1496/cr-13-c_az_seismic.pdf (last accessed November 2016).

Biasi, G. P., and J. G. Anderson (2007). Measurement of the parameter kappa, and reevaluation of kappa for small to moderate earthquakes at seismic stations in the vicinity of Yucca Mountain, Nevada, *Final Technical Report TR-07-007, Nevada System of Higher Education (NSHE)*, University of Nevada, Las Vegas, Nevada, 232 pp.

Biasi, G. P., and K. D. Smith (2001). Site effects for seismic monitoring stations in the vicinity of Yucca Mountain, Nevada, *MOL20011204.0045, A Report Prepared for the US DOE/University and Community College System of Nevada (UCCSN) Cooperative Agreement*.

Biro, Y., and P. Renault (2012). Importance and impact of host-to-target conversions for ground motion prediction equations in PSHA, *Proc. 15th World Conf. of Earthquake Engineering*, Lisbon, Portugal, 24–28 September, 10 pp.

Boore, D. M. (1983). Stochastic simulation of high-frequency ground motions based on seismological models of the radiated spectra, *Bull. Seismol. Soc. Am.* **73,** 1865–1894.

Boore, D. M., J. P. Stewart, E. Seyhan, and G. M. Atkinson (2014). NGA-West2 equations for predicting PGA, PGV, and 5% damped PSA for shallow crustal earthquakes, *Earthq. Spectra* **30,** 1057–1085.

Brune, J. N. (1970). Tectonic stress and the spectra of seismic shear waves from earthquakes, *J. Geophys. Res.* **75,** 4997–5002.

Brune, J. N. (1971). Correction, *J. Geophys. Res.* **76,** 5002.

Campbell, K. W. (2003). Prediction of strong ground motion using the hybrid empirical method and its use in the development of ground motion (attenuation) relations in eastern North America, *Bull. Seismol. Soc. Am.* **93,** 1012–1033.

Campbell, K. W. (2004). Erratum: Prediction of strong ground motion using the hybrid empirical method and its use in the development of ground-motion (attenuation) relations in eastern North America, *Bull. Seismol. Soc. Am.* **97,** 2418.

Campbell, K. W. (2009). Estimates of shear-wave Q and κ_0 for unconsolidated and semiconsolidated sediments in eastern North America, *Bull. Seismol. Soc. Am.* **99,** 2365–2392.

Campbell, K. W., and Y. Bozorgnia (2014). NGA-West2 ground motion model for the average horizontal components of PGA, PGV, and 5%-damped linear acceleration response spectra, *Earthq. Spectra* **30,** 1087–1115.

Chiou, B. S.-J., and R. R. Youngs (2014). Update of the Chiou and Youngs NGA model for the average horizontal component of peak ground motion and response spectra, *Earthq. Spectra* **30,** 1117–1153.

Chiou, B. S.-J., R. B. Darragh, N. Gregor, and W. J. Silva (2008). NGA project strong-motion database, *Earthq. Spectra* **24,** 23–44.

Edwards, B., D. Faeh, and D. Giardini (2011). Attenuation of seismic shear wave energy in Switzerland, *Geophys. J. Int.* **185,** 967–984.

Electric Power Research Institute (EPRI) (1993). *Guidelines for Determining Design Basis Ground Motions*, vols. 1/5, EPRI TR 102293, Electric Power Research Institute, Palo Alto, California.

Erickson, D., D. McNamara, and H. Benz (2004). Frequency dependent *Lg* Q within the continental United States, *Bull. Seismol. Soc. Am.* **94,** 1630–1643.

Frankel, A. (1982). The effects of attenuation and site response on the spectra of microearthquakes in the northeastern Caribbean, *Bull. Seismol. Soc. Am.* **72,** 1379–1402.

GeoPantech (2015). Southwestern United States Ground Motion Characterization SSHAC Level 3, *Technical Report Rev. 2*.

Goldstein, P., D. Dodge, M. Firpo, and L. Minner (2003). SAC2000: Signal processing and analysis tools for seismologists and engineers, in *The IASPEI International Handbook of Earthquake and Engineering Seismology*, W. H. K. Lee, H. Kanamori, P. C. Jennings, and C. Kisslinger (Editors), Academic Press, London, United Kingdom.

Hanks, T. C. (1982). $f_{\max}$, *Bull. Seismol. Soc. Am.* **72,** 1867–1879.

Hanks, T. C., and H. Kanamori (1979). A moment magnitude scale, *J. Geophys. Res.* **84,** 2348–2350.

Hough, S. E., and J. G. Anderson (1988). High-frequency spectra observed at Anza, California: Implications for Q structure, *Bull. Seismol. Soc. Am.* **78,** 692–707.

Humphrey, J. R., Jr., and J. G. Anderson (1992). Shear wave attenuation and site response in Guerrero, Mexico, *Bull. Seismol. Soc. Am.* **81,** 1622–1645.

Kamai, R., N. A. Abrahamson, and W. J. Silva (2013). Nonlinear horizontal site response for the NGA-West2 project, *PEER Report 2013/12*, Pacific Earthquake Engineering Research Center, University of California, Berkeley, California.

Kilb, D., G. Biasi, J. G. Anderson, J. Brune, Z. Peng, and F. L. Vernon (2012). A comparison of spectral parameter kappa from small and moderate earthquakes using southern California ANZA seismic network data, *Bull. Seismol. Soc. Am.* **102,** 284–300.

Kishida, T., R. Kayen, O.-J. Ktenidou, W. Silva, R. Darragh, and J. Watson-Lamprey (2014). PEER Arizona strong motion database and GMPEs evaluation, *Pacific Earthquake Engineering Research Center, PEER Report 2014/09, June 2014*, 170 pp., available at http://peer.berkeley.edu/publications/peer_reports/reports_2014/webPEER-2014-09-Arizona.pdf.

Ktenidou, O.-J., and N. Abrahamson (2016). Empirical estimation of high-frequency ground motion on hard rock, *Seismol. Res. Lett.* **87,** no. 6, doi: 10.1785/0220160075.

Ktenidou, O.-J., N. Abrahamson, S. Drouet, and F. Cotton (2015). Understanding the physics of kappa (κ): Insights from a downhole array, *Geophys. J. Int.* **203,** 678–691.

Ktenidou, O.-J., N. Abrahamson, W. Silva, and R. Darragh (2016). A methodology for the estimation of kappa (κ) for large datasets. Example application to rock sites in the NGA-East database, *Pacific Earthquake Engineering Research Center, PEER report 2016/01*, 117 pp., available at peer.berkeley.edu/publications/peer_reports/reports_2016/webPEER-2016-01-ktenidou.pdf (last accessed November 2016).

Ktenidou, O.-J., F. Cotton, N. Abrahamson, and J. G. Anderson (2014). Taxonomy of kappa: A review of definitions and estimation methods targeted to applications, *Seismol. Res. Lett.* **85,** 135–146.

Ktenidou, O.-J., C. Gelis, and F. Bonilla (2013). A study on the variability of kappa in a borehole. Implications on the computation method used, *Bull. Seismol. Soc. Am.* **103,** 1048–1068.

Laurendeau, A., F. Cotton, O.-J. Ktenidou, L.-F. Bonilla, and F. Hollender (2013). Rock and stiff-soil site amplification: Dependencies on V_{S30} and kappa (κ_0), *Bull. Seismol. Soc. Am.* **103,** 3131–3148.

Lermo, J., and F.-J. Chávez-García (1993). Site effect evaluation using spectral ratios with only one station, *Bull. Seismol. Soc. Am.* **83,** 1574–1594.

Muto, M., and Z. Duron (2015). High-frequency seismic hazard estimation and impact on seismic evaluation for dams, *presented at the Annual Meeting of SSA*, Pasadena, California.

Pacific Earthquake Engineering Research Center (PEER) (2015). NGA-East: Median ground-motion models for the Central and Eastern North America Region, *PEER Rept. No. 2015/04, Pacific Earthquake Engineering Research Center* http://peer.berkeley.edu/publications/peer_reports/reports_2015/webPEER-2015-04-NGA-East.pdf (last accessed November 2016).

Pacific Gas and Electric Company (PG&E) (1988). Final report of the Diablo Canyon long-term seismic program, *U.S. Nuclear Regulatory Commission Docket No. 50-275 and No. 50-323*.

Parolai, S., and D. Bindi (2004). Influence of soil-layer properties on k evaluation, *Bull. Seismol. Soc. Am.* **94,** 349–356.

Pasyanos, M. E. (2013). A lithospheric attenuation model of North America, *Bull. Seismol. Soc. Am.* **103,** 3321–3333.

Phillips, W. S., K. Mayeda, and L. Malagnini (2013). How to invert multi-band, regional phase amplitudes for 2-D attenuation and source parameters: Tests using the USArray, *Pure Appl. Geophys.* **171,** no. 3, 469–484, doi: 10.1007/s00024-013-0646-1.

Schneider, J., W. J. Silva, and C. Stark (1993). Ground motion model for the 1989 M 6.9 Loma Prieta earthquake including effects of source, path, and site, *Earthq. Spectra* **9,** no. 2, 251–287.

Silva, W., and B. Darragh (2014). Estimation of kappa, *Report Submitted to Pacific Northwest National Laboratory*, Richland, Washington.

Silva, W. J., N. Abrahamson, G. Toro, and C. Costantino (1997). Description and validation of the stochastic ground motion model, *Report Submitted to Brookhaven National Laboratory*, Associated Universities, Inc., Upton, New York, Contract No. 770573, available at http://www.pacificengineering.org/rpts_page1.shtml.

Van Houtte, C., S. Drouet, and F. Cotton (2011). Analysis of the origins of κ (kappa) to compute hard rock to rock adjustment factors for GMPEs, *Bull. Seismol. Soc. Am.* **101,** 2926–2941.

Van Houtte, C., O.-J. Ktenidou, T. Larkin, and C. Holden (2014). Hard-site κ_0 (kappa) calculations for Christchurch, New Zealand, and comparison with local ground motion prediction models, *Bull. Seismol. Soc. Am.* **104,** no. 4, 1899–1913.

Wessel, P., and W. H. F. Smith (1998). New, improved version of the Generic Mapping Tools released, *Eos Trans. AGU* **79,** 579.

Department of Engineering Science
University of Greenwich
Central Avenue, Chatham Maritime
Kent ME4 4TB, United Kingdom
(O.-J.K.)

Pacific Engineering and Analysis
El Cerrito, California 94530
(W.J.S., R.B.D.)

Pacific Gas & Electric Company
245 Market Street
San Francisco, California 94105
(N.A.A.)

Pacific Earthquake Engineering Research Center
University of California, Berkeley
Berkeley, California 94720
(T.K.)

Manuscript received 31 October 2015;
Published Online 10 January 2017;
Corrected Online 6 February 2017